Quaternary Science Reviews 202 (2018) 139–153

Contents lists available at ScienceDirect

Quaternary Science Reviews

journal homepage: www.elsevier.com/locate/quascirev

Environmental change during MIS4 and MIS 3 opened corridors in the Horn of Africa for *Homo sapiens* expansion☆

Finn A. Viehberg [a, *], Janna Just [a], Jonathan R. Dean [b, c, d], Bernd Wagner [a], Sven Oliver Franz [e], Nicole Klasen [f], Thomas Kleinen [g], Patrick Ludwig [h, i], Asfawossen Asrat [j], Henry F. Lamb [k], Melanie J. Leng [b, d], Janet Rethemeyer [a], Antoni E. Milodowski [l], Martin Claussen [g], Frank Schäbitz [m]

[a] *Institute for Geology and Mineralogy, University of Cologne, Zülpicher Straße 49A, 50674, Cologne, Germany*
[b] *NERC Isotope Geosciences Facilities, British Geological Survey, Nottingham, NG12 5GG, United Kingdom*
[c] *School of Environmental Sciences, University of Hull, HU6 7RX, United Kingdom*
[d] *Centre for Environmental Geochemistry, School of Biosciences, University of Nottingham, Sutton Bonington Campus, Leicestershire, LE12 5RD, United Kingdom*
[e] *Steinmann Institute for Geology, Mineralogy, and Palaeontology, University of Bonn, Nussallee 8, 53115, Bonn, Germany*
[f] *Institute of Geography, University of Cologne, Albertus-Magnus-Platz, 50923, Cologne, Germany*
[g] *Max Planck Institute for Meteorology, Bundesstr. 53, 20146, Hamburg, Germany*
[h] *Institute of Geophysics and Meteorology, University of Cologne, Pohligstraße 3, 50969, Cologne, Germany*
[i] *Institute for Meteorology and Climate Research, Karlsruhe Institute of Technology (KIT), Hermann-von-Helmholtz-Platz 1, 76344, Eggenstein-Leopoldshafen, Germany*
[j] *School of Earth Sciences, Addis Ababa University, P.O. Box 1176, Addis Ababa, Ethiopia*
[k] *Department of Geography and Earth Sciences, Aberystwyth University, Aberystwyth, SY23 3DB, United Kingdom*
[l] *Minerals and Waste Directorate, British Geological Survey, Nottingham, NG12 5GG, United Kingdom*
[m] *Institute of Geography Education, University of Cologne, Gronewaldstraße 2, 50931, Cologne, Germany*

ARTICLE INFO

Article history:
Received 28 February 2018
Received in revised form
3 September 2018
Accepted 4 September 2018
Available online 29 September 2018

ABSTRACT

Archaeological findings, numerical human dispersal models and genome analyses suggest several time windows in the past 200 kyr (thousands of years ago) when anatomically modern humans (AMH) dispersed out of Africa into the Levant and/or Arabia. From close to the key hominin site of Omo-Kibish, we provide near continuous proxy evidence for environmental changes in lake sediment cores from the Chew Bahir basin, south Ethiopia. The data show highly variable hydroclimate conditions from 116 to 66 kyr BP with rapid shifts from very wet to extreme aridity. The wet phases coincide with the timing of the North African Humid Periods during MIS5, as defined by Nile discharge records from the eastern Mediterranean. The subsequent record at Chew Bahir suggests stable regional hydrological setting between 58 and 32 kyr (MIS4 and 3), which facilitated the development of more habitable ecosystems, albeit in generally dry climatic conditions. This shift, from more to less variable hydroclimate, may help account for the timing of later dispersal events of AMH out of Africa.

1. Introduction

Anatomically modern humans (AMH) evolved in northern Africa and then eventually dispersed to populate the rest of the world (Hershkovitz et al., 2018; Hublin et al., 2017; Mallick et al., 2016; Pagani et al., 2016). There is a consensus that climate change was a possible driver of early dispersal events (Breeze et al., 2016; Groucutt et al., 2015; Timmermann and Friedrich, 2016). Shifts in hydroclimate, causing large-scale environmental change and consequent habitat loss or expansion, may influence demographic growth and dispersal success (Potts and Faith, 2015). In this context, regional wildlife communities, which were potential food sources for AMH, also changed their species composition and abundances

☆ F.A.V., J.J., J.R.D. wrote the manuscript with the support of all co-authors. F.A.V., J.J., J.R.D., B.W. M.J.L., and F.S. supervised the study. F.A.V., J.J., J.R.D., S.O.F., N.K., J.R. and A.E.M. performed geological and/or chronological analyses. F.A.V., T.K., P.L. and M.C. performed numerical analyses. A.A., H.F.L. and F.S. collected the core.

* Corresponding author.
E-mail address: finn.viehberg@uni-koeln.de (F.A. Viehberg).

https://doi.org/10.1016/j.quascirev.2018.09.008

as vegetation types adapted to the prevailing climate conditions (Assefa et al., 2008; Jónsson et al., 2014).

Climatic and environmental changes over the past 150 kyr for this region has so far been inferred from data from often discontinuous lacustrine deposits, speleothems and stromatolites (Blome et al., 2012; Lamb et al., 2018), and from distant marine sediment cores from the eastern Mediterranean, Red and Arabian Seas (Blome et al., 2012; Deplazes et al., 2013; Ehrmann et al., 2016; Tierney et al., 2017). The sediment record from Lake Tana at the northern edge of the Ethiopian Highlands (Costa et al., 2014) shows that the regional climate is driven by the interplay between the dynamics of two complex atmospheric circulation systems, the West African Monsoon (WAM) and the East African Monsoon (EAM), forced by variation in climatic precession and/or solar insolation (Mohtadi et al., 2016; Omondi et al., 2012; Trauth et al., 2001; Weldeab et al., 2007, 2014). The WAM transports and recycles moisture inland from the Atlantic Ocean, the Congo Basin and the Sudd Basin to east Africa (Weldeab et al., 2007). The incursion of the WAM into northeast Africa is strongest during the northern hemisphere summer, because of the northernmost position of the Intertropical Convergence Zone (ITCZ), associated with the strong Saharan Heat Low and the dominance of the opposing EAM resulting in a long rainy season ('*Kiremt*') (Diro et al., 2011; Weldeab et al., 2007). The EAM is linked to the South Asian Monsoon system and shows two seasonal aspects. Moist air masses move from the Indian Ocean to equatorial eastern Africa beginning in the spring of the northern hemisphere and continue to flow from south to north along the Ethiopian Rift System and result in a short but intense rainy season ('*Belg*') (Diro et al., 2011). During the northern winter season, dry air masses initially flow from the Arabian Peninsula parallel to the east African coast in the opposite direction. The ITCZ and the convection over the warm water masses of the Indian Ocean Dipole are the main driver of the EAM and equally limit its geographical extension (Diro et al., 2011; Weldeab et al., 2014). It is proposed that the interoceanic confluence passage of WAM and EAM, the Congo Air Boundary, swings towards the east of the Ethiopian Highlands during periods of high insolation maxima, leading to a strengthening of the WAM and producing a prolonged and stronger rainy season in northeast Africa, leading to lake level high stands (Costa et al., 2014; Junginger et al., 2014).

The catchment of Chew Bahir (~32,400 km^2) drains parts of the Southwestern Ethiopian Highlands (Fig. 1a). This orographic barrier received exceptional amounts of precipitation during North African Humid Periods in the late Pleistocene (Ehrmann et al., 2016) making Chew Bahir an amplifier lake that is sensitive to hydrological changes (Street-Perrott and Harrison, 1985; Teller and Last, 1990). Sediment sequences from Chew Bahir record the past regional hydroclimate signal that is essential to assess the shifts in palaeoenvironment during the postulated Human Migration Waves by Human Dispersal Models (Timmermann and Friedrich, 2016).

Here we present a near continuous lacustrine sediment record from 116 kyr ago from close to the earliest known fossil *Homo sapiens* site in eastern Africa and thus at a gateway to a corridor region for human migration waves to sites out of Africa. Our study fills a crucial gap in available long palaeoenvironmental archives from the Horn of Africa, allowing a better understanding of the environmental context for AMH dispersal from northeastern Africa. The data are essential to challenge outputs of new and existing earth and climate system models in terms of moisture availability and landscape vulnerability.

1.1. Study area

The playa mudflats of Chew Bahir (970 km^2) lie at 500 m above sea level (asl) and are sporadically flooded by a few decimetres of water during the rainy seasons in spring ('*Belg*') and summer ('*Kiremt*'). In the late 19th century, a maximum lake water depth of up to 8 m was documented (Grove et al., 1975). Chew Bahir is located in the Broadly Rifted Zone between the Main Ethiopian Rift (MER) and the Kenya-Turkana Rift and is filled with up to 5 km of sediment (Cohen et al., 2016; Foerster et al., 2012; WoldeGabriel and Aronson, 1987). It is a failed rift marking the transition between the active MER to the north and the Turkana Basin to the south (Ebinger et al., 2000; WoldeGabriel and Aronson, 1987). The basin's overspill in the south at approx. 540 m asl drains to the Turkana basin and limits the maximum extension of the lake surface to 2390 km^2 (Fig. 1a) (Lehner and Grill, 2013). The geology of the Chew Bahir Rift is composed of Precambrian granitic and mafic gneisses and granites in the north and west, by, and of Miocene basalts and trachytes in the Teltele-Konso range to the east (Davidson, 1983). Oligocene basalt flows with subordinate rhyolites, trachytes, tuffs and ignimbrites cover the Precambrian basement units in the northern parts of the Weyto catchment (Corti, 2009; Corti et al., 2013a, 2013b; Keir et al., 2015; Roberts et al., 2012; Vétel et al., 2005; WoldeGabriel and Aronson, 1987). The total catchment (~32,400 km^2) is divided into a larger regional catchment drained by the Sagan river including the Ethiopian Rift lakes, Lake Abaya and Lake Chamo (~22,000 km^2) and a local catchment in the northwest drained by the Weyto river (~7000 km^2) (Fig. 1a) (Lehner and Grill, 2013). The extensive catchment connects the generally cooler Ethiopian highlands in the north with the hotter and drier lowlands (Fig. 1a) and hence different seasonal precipitation patterns account for the hydrology of the Chew Bahir basin (Nyssen et al., 2004). The two main rivers enter the Chew Bahir basin in the north and develop an extensive avulsion belt in the floodplains. Minor streams form alluvial fans on the foothills of the rift shoulders, the Hammar Range in the west and the Teltele Plateau in the east (Lehner and Grill, 2013).

2. Materials and methods

2.1. Coring operation and core handling

The coring site HSPDP-CHB-1A (N 4.7071°, E 36.8524°; Fig. 1a) is situated in the central most part of the Chew Bahir basin, being accessible and suitable for using land-based drilling equipment during 18th-24th March 2014. We used a rotary single tube drill operated by Addis Geosystems Ltd. with subsequent casing to a depth of 29 m below lake floor (mblf). The hole remained stable to the last core section taken at a depth of ~40 mblf. The core tube (inner diameter 86 mm and 76 mm) itself was 200 cm long while the maximum protruding length was 180 cm per core run to ensure continuous material supply. The consecutive core material was extruded and described in the field. The core was taken to the University of Cologne, Germany, and cut into a working half and an archive half. On opening the working halves were described for lithology and sediment colour.

2.2. XRF scanning, carbon concentration, and grain-size analyses

The working half cores were line-scanned by an X-ray fluorescence (XRF) Itrax Core Scanner (Cox Analytical Systems Ltd., Sweden) equipped with a Cr-source set to 30 kV and 30 mA, at a spatial resolution of 0.25 cm and a scanning time of 10 s per measurement. The specific element counts were normalised to the total element counts prior to further data processing. Eventually, the working halves were continuously sampled in 2 cm thick consecutive segments and freeze-dried. Prior to further analyses, carbonate nodules >5 mm were separated from the sediment aliquots and counted. Total carbon (TC) concentrations were measured at a

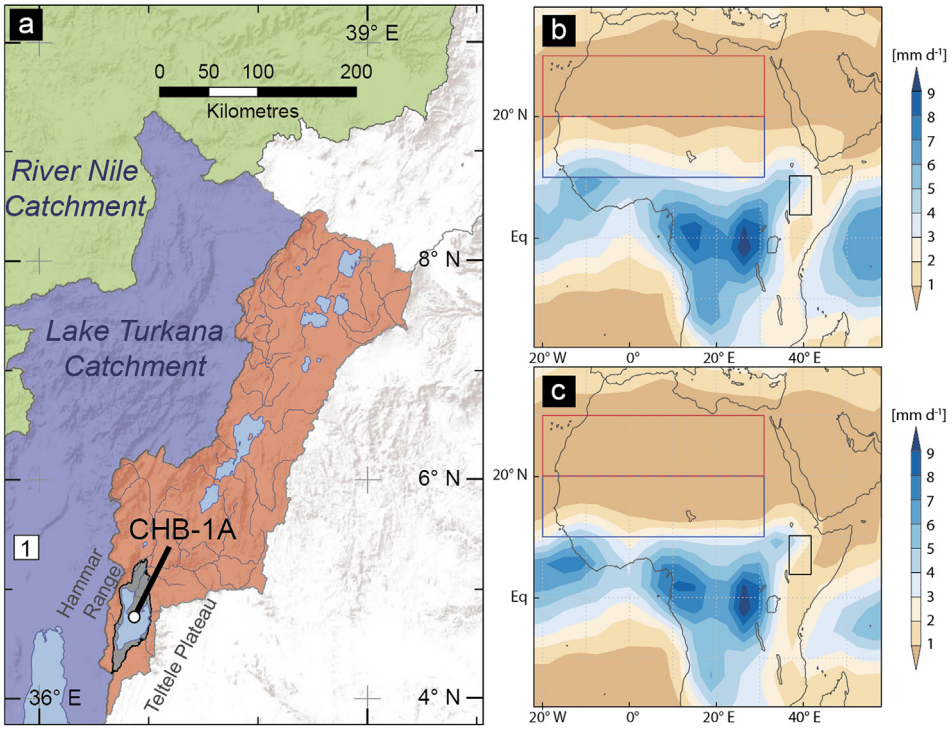

Fig. 1. Present hydrological setting of the study site and reference sites used in the text. (a) Red area covers the extended catchment of the Chew Bahir basin, violet area plots the catchment of Lake Turkana, green area represents the catchment of the River Nile, the line points to the position of the core locality CHB-1A, grey shows the maximum lake extension of Chew Bahir at 540 m (above sea level) asl, light blue shows the Chew Bahir area at 501 m asl., 1: Omo-Kibish formation type locality for *Homo sapiens*. Mean annual precipitation (mm d^{-1}) as obtained from NorESM time slice model runs for: (b) under low precession forcing at 115 kyr and (c) under high precession forcing at 125 kyr. Red (blue) rectangle represents CLIMBER2 grid cells for Sahara (Sahel) zone (see text). Black box marks maps excerpt depicted in (a).

10 cm resolution with an elemental analyser (vario MICRO cube, Elementar Ltd.). In the same interval, total inorganic carbon (TIC) and total carbon (TC) were analysed by thermic-catalytic oxidation using a nondispersive infrared sensor (Dimatoc, 2000; Dimatec Ltd.). The content of total organic carbon (TOC) was then calculated as the difference between TC and TIC.

At 20 cm resolution, the grain size composition was determined using a Laser Diffraction Particle Size Analyser (Beckman Coulter LS13 320, Beckman Coulter, Inc.) at the Institute of Geography, University of Cologne, Germany. Samples were pre-treated with H_2O_2 (30%), HCl (10%) and 1.0 M NaOH to remove organic carbon, inorganic carbonate and biogenic opal, respectively. For aggregate dispersion, the samples were placed on a shaker for 12 h and then underwent one minute of ultrasonic treatment, adding $Na_4P_2O_7$ and $Al_2(SO_4)_3$. Statistical measures were calculated using GRADISTAT (Blott and Pye, 2001).

2.3. Ostracod analyses

At 20 cm intervals, >10 g freeze-dried sediment was weighed with an analytical balance (Sartorius AG, Germany), dispersed in 3% HClO at 40 °C for 1 h, wet sieved on a 150 μm mesh screen and thoroughly washed with deionized water. The remaining fraction was again freeze-dried and sorted for ostracod remains under a dissecting microscope. Ostracod valves were counted and identified for further palaeoenvironmental interpretation (Lindroth, 1953; Martens, 1984, 1990). If a sample yielded fewer than 300 valves, all valves were counted. Carapaces were counted as two valves. The counts are standardised to 10 g dry sediment.

2.4. Mineralogy

Mineral identification and semi-quantitative analyses were undertaken on samples from three depth-intervals at 20 cm (144.0–601.5 cm and 1100.0–1498.5 cm) and 40 cm (2438.1–3348.1 cm) resolution, respectively. Dry powdered bulk sediment samples were determined by X-Ray Diffraction (XRD) using Bruker AXS D8 Advance with automatic slit and Ni-filtered Cu-Kα radiation at Steinmann Institute, University of Bonn (operation conditions: generator voltage (kV): 30, generator current (mA): 40, scan range (°2Θ): 4–70, step size (°2Θ): 0.04, counting time (s): 2, divergence slit: variable (v20), anti-scatter slit: variable (v20), detector slit: 0.2 mm). Mg contents in calcite were determined from the $d_{(10.4)}$ diffraction spacing shift using the idealized curve of Goldsmith and Graf (1958). For detailed analyses, thin-sections of nodules and bulk sediment samples were analysed by backscattered electron imaging secondary electron imaging, respectively, using a FEI Quanta 600 Environmental Scanning Electron Microscope (ESEM) equipped with an Oxford Instruments INCA Energy 450 energy-dispersive X-ray microanalysis (EDXA) system at the British Geological Survey, UK.

2.5. Oxygen and carbon isotopes

Endogenic calcite (excluding the nodules) in the bulk sediment samples was analysed for oxygen ($\delta^{18}O$) and carbon ($\delta^{13}C$) isotope composition using the classical vacuum technique excluding dolomite (Dean et al., 2015) and a Thermo Finnigan MAT 253 mass spectrometer at the NERC Isotope Geosciences Facilities, UK. Data are given as per mil (‰) deviations from VPDB and analytical

reproducibility was <0.1‰ for $\delta^{18}O$ and $\delta^{13}C$ based on standard materials.

2.6. Radiocarbon and optically stimulated luminescence and dating

Bulk sediment samples were chosen for radiocarbon dating, as suitable discrete material was not found. The sample preparation followed the standard procedure (Rethemeyer et al., 2013) and the measurements were carried out with the accelerator mass spectrometer at the University of Cologne, Germany (Cologne AMS).

Polymineral fine grain samples (4–11 μm) were extracted using conventional sample preparation techniques (Frechen et al., 1996). All measurements were carried out on an automated Risø TL/OSL DA 20 reader equipped with a calibrated ^{90}Sr beta source using the post-infrared infrared stimulated luminescence signal measured at 290 °C ($pIRIRSL_{290}$, Thiel et al., 2011). Stimulation was carried out with infrared diodes (870 nm, FWHM = 40) and the signals were detected through an interference filter (410 nm). The initial 4 s of the signal minus a background of the last 20 s was used for p-IRIRSL dating. Laboratory experiments included prior-IR stimulation temperature tests (Buylaert et al., 2012) using a range of temperatures from 50 to 260 °C and preheat plateau dose recovery tests. For theses dose recovery tests, the samples were illuminated for 24 h in a Hönle SOL2 solar simulator and a laboratory dose in the range of the natural dose was given to the samples. Subsequently, the prior IR stimulation temperature was kept constant at 50 °C and the post-IRIR stimulation tracked the preheat temperature by −20 °C-. The apparent residual dose after 24 h bleaching in the solar simulator was measured using routine measurements (Thiel et al., 2011). Samples C-L3918 and C-L3867 were taken from two adjacent samples from the same depth as an internal check on reproducibility.

Data analyses were performed using the Risø Luminescence Analyst software (version 4.10). Equivalent doses were calculated with an arithmetic mean. The radionuclide concentrations were measured with high resolution gamma ray spectrometry. The dose rate was calculated using conversion factors of Guérin et al. (2011) and the measured water content. The internal beta dose rate contribution of the polymineral fine grain samples was calculated by assuming a potassium content of 12.5 ± 0.5% (Huntley and Baril, 1997). Alpha and beta attenuation factors of Bell (1980) and Brennan (2003) were used. The cosmic dose rate was calculated following Prescott and Hutton (1994).

2.7. Palaeomagnetic analyses

For palaeomagnetic sampling and analyses, the sediment was sampled in oriented 6.2 cm^3 plastic boxes. Samples were analysed continuously in ~2.5 cm intervals down to 28.60 m depth and below at 6 cm intervals. Disturbed sediments were excluded from analysis. In total 950 (averaged resolution of ~4.2 cm), samples were measured. Volumetric magnetic susceptibility (κ) was calculated, using a KLY2 Kappabridge.

Natural and artificial remanence parameters were measured on a 2G 755R cryogenic magnetometer at the University of Bremen, Germany. Demagnetization of Natural Remanent Magnetisation (NRM) was conducted in 12 incremental steps (0 mT–100 mT). Anhysteretic Remanent Magnetisation (ARM) was imparted with a 100 mT AF and 50 μT DC field and subsequently demagnetized in 9 steps (0 mT–100 mT). The ratio of NRM and ARM demagnetization of the 30 mT step was used as a proxy for the relative palaeointensity (RPI).

2.8. Comparison to the lake Malawi Ca record

To compare our Chew Bahir data to the 120 kyr Ca record from Lake Malawi (Lyons et al., 2015; Scholz et al., 2007, 2011) we corrected the published age-depth model of Lake Malawi to account for the finding of the Youngest Toba Tuff (YTT) (Lane et al., 2013). We developed a simplified age model for the relevant core MAL05-1C and adopted the published radiocarbon ages (Scholz et al., 2011) in the interval 0.0 to 21.053 mblf corresponding to 0–50.457 kyr BP, respectively. Furthermore, two additional age control points were inserted at 28.10 mblf, (YTT; ~75.0 kyr), and 67.25 mblf, (palaeomagnetic inclination; 'Blake event' at 122.5 kyr). A linear sedimentation rate was presumed between the oldest radiocarbon age and each additional control point as accomplished in previous studies (Lyons et al., 2015).

2.9. Breakpoint analysis

We performed breakpoint analyses on the main geochemical and geophysical proxy datasets from core HSPDP-CHB-1A (K/Ti, Ca/Ti, $\delta^{18}O$) described here. Each dataset was separately imported as a time series in the software package R including the library *strucchange* (R Core Team, 2016; Zeileis et al., 2003; Zeileis et al., 2002) to analyse significant fluctuation changes in regression relationships over time. A 95% confidence interval is given for the time of significant proxy fluctuations.

2.10. Model simulations

Data from different climate model simulations were consulted to receive an overview of the spatial distribution and temporal evolution of the precipitation regime over Africa. Precipitation data from time slice experiments (125 kyr, 115 kyr; each 100 years of data available) covering the last interglacial (Langebroek and Nisancioglu, 2014) are consulted to analyse the effects of the orbital precession on the different spatial precipitation distribution over Africa.

Since complex earth system models are not yet capable to simulate a full glacial cycle, additional model simulations were carried out with an Earth System Model of Intermediate Complexity, CLIMBER2 (Ganopolski et al., 2001; Petoukhov et al., 2000). The model consists of a 2.5-dimensional statistical-dynamical atmosphere with a latitudinal resolution of 10° and a longitudinal resolution of roughly 51°, an ocean model resolving three zonally averaged ocean basins with a latitudinal resolution of 2.5°, a sea ice model, and the dynamic terrestrial vegetation model VECODE (Brovkin et al., 2002).

The model experiment spans the time 126 kyr BP to 0 BP, and is driven with orbital changes and prescribed greenhouse gases, as well as ice sheet extent diagnosed from an earlier experiment including the ice sheet model SICOPOLIS (Ganopolski et al., 2010). The precipitation threshold for full desert conditions in VECODE is set to $0.6*10^{-5}$ kg m^{-2} s^{-1}. The relevant grid cells of Sahel and Sahara were selected to estimate the temporal evolution of the precipitation regime and vegetation coverage at the study area under the given model parameters.

3. Results

3.1. Core and sediment characteristics

Data from core sections of drill site HSPDP-CHB-1A (Fig. 1a) were spliced to produce a composite profile that consists of 3789 cm of sediments that were recovered up to a maximum drilled depth of 40.69 mblf, equating to 93% recovery. The

laboratory length measured supersedes the drilling data based on field depth given in previous reports (Cohen et al., 2016). Initial results from analyses of total carbon species (organic and inorganic; TOC resp. TIC) and total nitrogen (TN) from sample intervals of every 10 cm revealed that the material has very low TOC (mean < 0.67%) and TN (mean < 0.02%). Attempts to extract plant wax compounds from test samples with the highest TOC content with standard methods (Castañeda et al., 2010; Collins et al., 2014) returned an insufficient amount for reliable analyses.

The mineralogy of the core material is dominated by calcite and the silicate mineral analcime. SEM imaging of samples through the core sequence confirm that many of the calcite grains are fine euhedral rhombs, as would be expected of endogenic precipitates as opposed to a fragmental detrital and anhedral diagenetic calcite (Figs. SI-1 & SI-2; Kelts and Hsü, 1978; Leng et al., 2010; Talbot and Kelts, 1986). Analcime is a natural zeolite that can be formed authigenically from detrital silicates, such as illite/smectite, in high alkaline (pH > 9) pore waters that often develop in hydrologically closed basins (Fig. SI-1) (Gall and Hyde, 1989; Langella et al., 2001; Singer and Stoffers, 1980).

The sediment sequence was subdivided into two major lithozones (Fig. 2). Lithozone 1 (LZ1; 4069-1370 cm) consists mainly of medium-grained silt and shows a high grain size variability (mean 27.1 ± 24.4 μm). The sediment is intercalated with lithified carbonate layers or fine-sand beds (Fig. 2). Nodules (5 to >20 mm) of dolomite and/or high-Mg and high-Mn calcite occur sporadically in the sediment with increased abundance from 3948 to 1994 cm (Fig. 2).

Based on cyclic alternation of high (low) total inorganic carbon (TIC) concentrations and simultaneous Ca/Ti and to a lesser degree K/Ti peaks (troughs), co-occurring with low (high) magnetic susceptibility and fine (coarse) grain size, LZ1 can be subdivided in five zones (LZ1A 4069-3175 cm, LZ1B 3175-2537 cm, LZ1C 2537-2120 cm, LZ1D 2120-1709 cm and LZ1E 1709-1370 cm).

Lithozone 2 (LZ2) shows moderate Ca/Ti or K/Ti and TIC concentrations, with lower amplitudinal variations. The segment consists mainly of fine silt (mean 9.2 ± 3.8 μm) and a few fine-sand beds, which are intercalated in the sedimentary sequence (Fig. 2). LZ2 K/Ti has a notable minimum at 543 cm; here analcime and illite/muscovite follow the general potassium trend (Fig. 3).

3.2. Stable isotopes

Throughout the core, $\delta^{18}O$ data from endogenic calcite show a total variation of nearly 17‰ (Fig. 2). The period from the base of the core sequence up to ~3890 cm (Fig. 2) shows a rapid shift from the lowest $\delta^{18}O$ (min −5.8‰), to a period of higher and more stable $\delta^{18}O$ (average + 2.4‰) until ~3175 cm (end of LZ1A). This is followed by an interval to 2639 cm that is characterised by a major excursion to higher $\delta^{18}O$ (max +7.2‰) and a subsequent shift to low $\delta^{18}O$ (min −2.9‰). Below and above a consolidated calcite layer at ~2530 cm (end of LZ1B) the values swing rapidly between high $\delta^{18}O$ (max +5.7‰) and low $\delta^{18}O$ (min −0.9‰). At 2367 cm, a shift to higher $\delta^{18}O$ (average + 3.4‰) lasts until ~1790 cm. There is then a shift to lower $\delta^{18}O$ (1786-1746 cm; average −1.3‰) followed by a

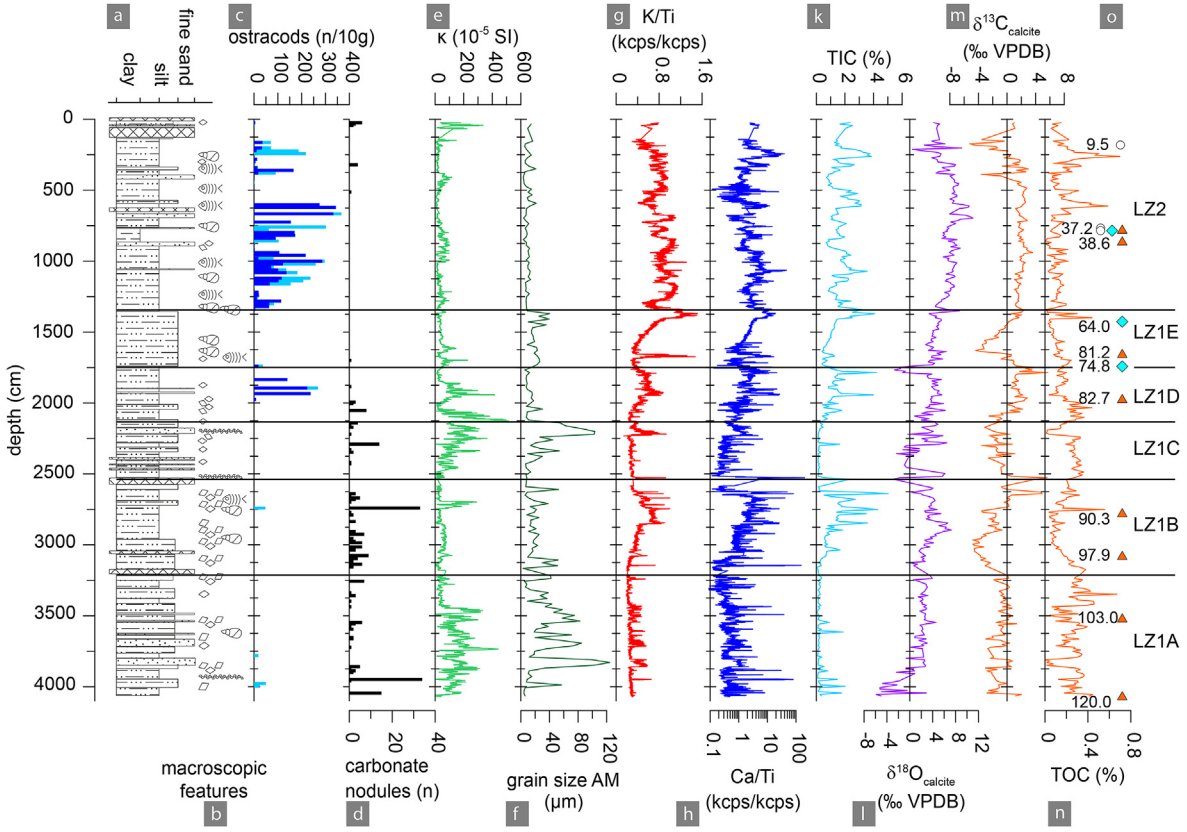

Fig. 2. Lithostratigraphy and proxies from Chew Bahir core HSPDP-CHB-1A plotted vs. core depth. (a) Stratigraphical column with grain size classes. (b) Macroscopic biological and mineral remains. (c) Ostracod valves standardised to 10 g dry-sediment; total sum (blue); *Limnocythere* cf. *borisi* (black) (d) Carbonate nodules counted per sample. (e) Magnetic susceptibility. (f) Arithmetic mean of grain size. (g) K/Ti ratio from scanning X-ray fluorescence (kcps = thousand counts per second). (h) Ca/Ti ratio from scanning X-ray fluorescence. (k) Total inorganic carbon (TIC) content from dry sediment. (l) $\delta^{18}O$ of endogenic calcite. (m) $\delta^{13}C$ of endogenic calcite. (n) total organic carbon (TOC) content from dry sediment. (o) Tie points in the age-depth model: radiocarbon bulk samples (open circle), luminescence samples (orange triangle), and relative palaeointensity correlation to GLOPIS (cyan diamond) (ages in kyr BP).

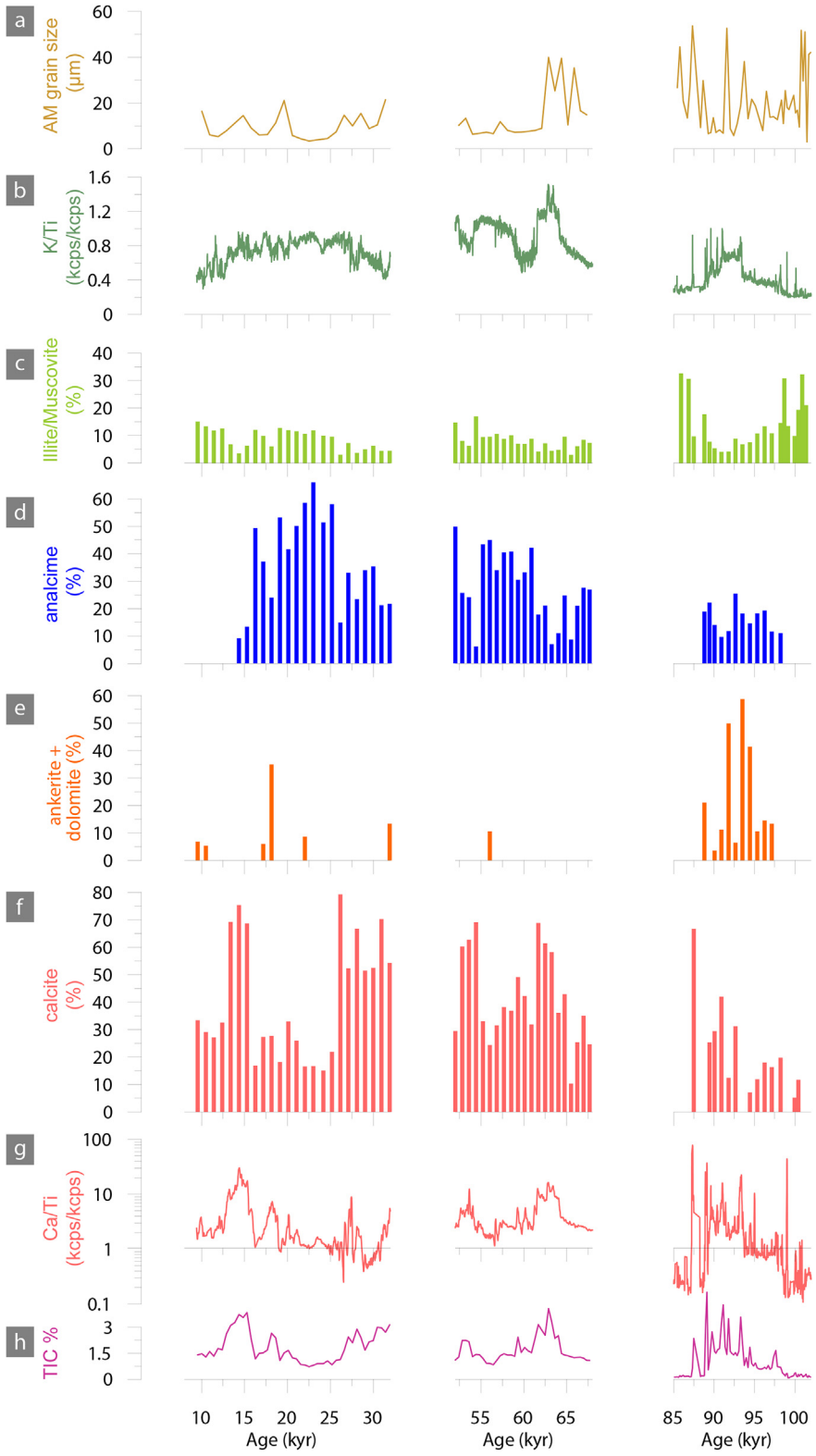

Fig. 3. Comparative core sections (A: 9.6–31.9 kyr, B: 52.0–67.7 kyr, C: 85.9–101.4 kyr) with results on detailed mineralogy, grain size distribution, element ratios and TIC. Arithmetic mean in grain size distribution (AM grain size), K/Ti ratio from XRF data (K/Ti), Illite/Muscovite (%), Analcime (%), Ankerite/Dolomite (%), Calcite (%), Ca/Ti ration from XRF data, and TIC (%).

period of relatively stable $\delta^{18}O$ (average + 4.3‰) that ends ~1370 cm (end of LZ1E), when there is a peak at ~1350 cm (+8.7‰). The subsequent period has high $\delta^{18}O$ values (average + 7.3‰) lasting to 310 cm, interrupted by two peaks centred on ~690 and 620 cm (+11.0‰ and +10.4‰ respectively). Between 310 cm and the core top, the isotope values fluctuate rapidly between high $\delta^{18}O$ (max +9.0‰) and low $\delta^{18}O$ (min +0.5‰).

While there are some similarities between the $\delta^{18}O$ and $\delta^{13}C$ values, there are also substantial differences (Fig. 2). $\delta^{13}C$ fluctuates periodically by several per mil in the period from the base of the core until ~3500 cm (max +2.0‰ at 4055 cm, min −3.0‰ at 3869 cm) before more stable values between ~−0.5‰ and +0.5‰ until ~3266 cm. After this, there is a shift to some of the lowest values in the record (min −4.8‰ at 2966 cm) and then a rise to higher values ~2900 cm. After a relatively stable period until ~2750 cm, there is a rise to ~0‰ but with two peaks to higher values (highest +5.6‰ at 2527 cm). Values then return to ~ −1.5‰ until ~2070 cm, before rising to between ~0‰ and +3‰ for most of the period until ~1650 cm, albeit with a number of peaks again (max +5.7‰ at 1786 cm, at the time of very low values $\delta^{18}O$). Values then decrease rapidly to a low of −4.4‰ at 1628 cm and then rise (at the same time as a less dramatic rise in $\delta^{18}O$) to ~+1‰ to +2.5‰ for the most stable period of the record from ~1400 cm to ~450 cm, at the time of stability in the $\delta^{18}O$ record. As with the $\delta^{18}O$ record, there are rapid fluctuations between higher (max +3.0‰) and lower (min −5.2‰) values to the top of the core.

3.3. Biological proxies

The ostracod record of Chew Bahir is dominated by four ostracod species: *Limnocythere* cf. *borisi, Darwinula stevensoni*, *Ilyocypris* sp., and *Heterocypris giesbrechti* (Fig. 4). The species are members of halotolerant genera (De Deckker, 1981; McKenzie, 1971) that are also found in modern lake ecosystems within the Chew Bahir catchment (Martens, 1990; Martens and Tudorancea, 1991). *L.* cf. *borisi,* especially, has fragile valves that are very well preserved in most samples where it is present. In addition, an abundant record of assorted juvenile instars is also found in the described thanatocoenoses. Ostracod valves occur only sporadically in LZ1 (Fig. 2). In the upper zone of LZ1C (1933–1835 cm) there is an abundant and partly monospecific faunal assemblage dominated by *L.* cf. *borisi*. In LZ2, the ostracod record is more stable. Two gaps with no or poorly preserved ostracod valves occur (at 601-380 cm and 144-0 cm). Shell fragments of aquatic gastropod and fish bones occur sporadically throughout the core, but are more frequent in LZ2 (see Fig. 2). Pollen and diatom remains are not preserved continuously in the sediment record.

3.4. Bayesian age-depth model from radiocarbon, optically stimulated luminescence (OSL) and palaeomagnetic ages

Results of previous studies from Chew Bahir sediments produced critical radiocarbon age estimates, which follow no systematic trend, with diagenetic and reservoir effects on biogenic carbonate being the likely explanation (Foerster et al., 2012, 2014). We evaluated the estimated radiocarbon ages of three bulk samples from HSPDP-CHB-1A, because of their generally low organic carbon content. The two lower most ^{14}C dates show unexpectedly high $\delta^{13}C$ values for bulk organic matter (>2.3‰) and hence these were excluded from the final age-model (Table 1).

In addition, nine samples through the sediment core were selected for luminescence dating using post infrared infrared stimulated luminescence dating (p-IR IRSL) that was applied to polymineral fine grains. The laboratory experiment using different prior-infrared stimulation temperatures indicated a plateau between 50 and 140 °C for sample C-L3863, between 50 and 220 °C for C-L3866, between 80 and 180 °C for C-L3867, between 50 and 125 °C for C-L3869 and between 50 and 110 °C for C-L3870 (Fig. SI-4). Prior-IR stimulation temperatures above 200 °C reduced the p-IR IR_{290} signal significantly. Finally, the lowest prior IR stimulation temperature of the plateau range was used for further measurements. Laboratory doses were successfully recovered for samples C-L3866, C-L3867, C-L3869 and C-L3870 (Fig. SI-5, Table 2). In another dose recovery experiment, laboratory doses for samples C-L3863 and C-L3864 were successfully recovered for p-IR IR stimulation, which tracked the preheat temperature by −20 °C (Fig. SI-6, Table 2). Only a small residual dose of 2–4 Gy was left after 24 h of bleaching in the Hönle Sol2 solar simulator. The luminescence age estimates were between 37 and 120 kyr (Table 3).

A first age-depth approximation was based on the accepted radiocarbon age and nine luminescence ages. Subsequently, these age control points were iteratively shifted within the error of the individual ages to fit general patterns in our relative palaeointensity (RPI) record with regional RPI data from the Somali Basin (Meynadier et al., 1995). To further refine our age model, we correlated minima and maxima in our RPI record to available palaeomagnetic data from Chew Bahir (Trauth et al., 2015), the high resolution global relative palaeointensity stack (GLOPIS, Laj et al., 2013), and the RPI data from ODP site 984 (Channell et al., 2002) from the Iceland Basin (Fig. SI-7). The inclusion of only three additional correlation points within the uppermost 20 m showed a strong correspondence of our data and the reference records. Two minima in our RPI record were assigned to globally known palaeomagnetic excursions (see Table 3).

The final age-depth model is based on one radiocarbon age, nine luminescence ages and three tie-points derived from the correlation of RPI record (see Fig. 5, Table 3). We used a Bayesian model approach to determine the most likely age-depth curve using the Bacon software (Blaauw and Christen, 2011) and the INTCAL13 data set (Reimer et al., 2013). We presumed a dynamic setting for the sediment accumulation rates and chose a step size of 15 cm segments to estimate the ages. The age-depth model reveals a mean sedimentation rate of ~46 cm/kyr in the interval 4068-1370 m, relative to a mean sedimentation rate of ~25 cm/kyr in the top part.

4. Discussion

4.1. Interpretation of proxies

From the sedimentological evidence, we interpret the XRF scanning data in terms of elemental ratios. Ti is a commonly inert and immobile element that occurs in a variety of mineral phases, therefore we use it as proxy for clastic sediment supply, e.g. of fluvial (Haug et al., 2001) or aeolian (Yancheva et al., 2007) input. K is also a ubiquitous element that is biocycled and easily leached from soils as a water-soluble cation (Stiles et al., 2003). It is also substituted in many mineral phases due to physical weathering, or fixed in clay-complexes (Arnaud et al., 2012; Foerster et al., 2012, 2018; Langella et al., 2001) and therefore often bound to the fine grain size fraction (Cuven et al., 2010). In the hydrological setting of the Chew Bahir basin, we use increased K/Ti ratio as indicator for deposition of physically weathered minerals during periods of enhanced erosional fluvial input from a less vegetated arid catchment and/or K-enrichment due to authigenic mineral formation, i.e. illitization of smectites in a hydrologically closed system when alkalinity and salinity are high (Foerster et al., 2018). In contrast, decreased K/Ti ratio indicates reduced deposition of detrital material during more vegetated conditions of wetter climate when K is dispersed in a hydrologically open system or not enriched in mineral phases.

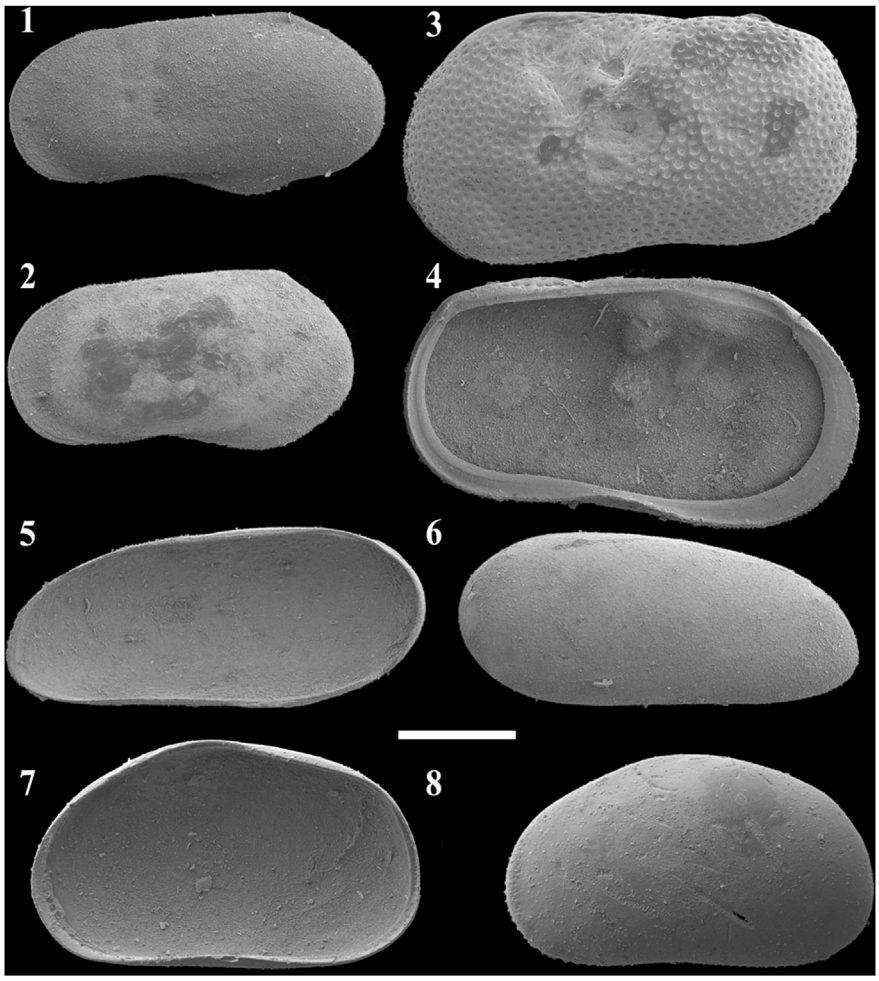

Fig. 4. Dominant ostracods from Chew Bahir core HSPDP-CHB14-1A. 1: *Limnocythere* cf. *borisi*, male, left valve (LV), exterior. 2: *Limnocythere* cf. *borisi*, female, LV, exterior. 3: *Ilyocypris* sp., female, LV, exterior. 4 *Ilyocypris* sp., female, LV, interior. 5: *Darwinula stevensoni*, female, right valve (RV), interior, 6: *Darwinula stevensoni*, female, RV, exterior, 7: *Heterocypris giesbrechti* female, RV, interior, 8: *Heterocypris giesbrechti* female, LV, exterior; scale bar = 200 μm (1–6) and 300 μm (7 & 8).

Table 1
AMS radiocarbon dates and $\delta^{13}C$ from Chew Bahir core HSPDP-CHB-1A, measured at the AMS Cologne facility, in Cologne, Germany. Laboratory identifier (Lab Code), sample depths, materials chosen as well as radiocarbon ages and calendar ages are given. The radiocarbon ages of all samples were calibrated into calendar years before present (kyrs cal BP) using the INTCAL13 calibration curve (Reimer et al., 2013). mblf = meters below lake floor.

Lab code	Sample depth (mblf)	material	^{14}C age (yrs BP)	error (yrs)	$\delta^{13}C$ (‰)	TOC (%)	calendar age (kyr cal BP)
COL2915.1.1	1.440	bulk	8573	51	−11.8	0.22	9.51–9.58
COL2916.1.1	7.345	bulk	33,103	268	3.1	0.14	36.88–38.26
COL2917.1.1	7.595	bulk	29,259	191	2.3	0.10	33.37–34.01

Analcime is particularly abundant throughout the core. This is a natural zeolite that can form authigenically by reaction of detrital silicates, such as illite/smectite, with highly alkaline (pH > 9) pore waters that often develop in hydrological closed systems, and which may absorb K ions (Fig. 3) (Gall and Hyde, 1989; Langella et al., 2001; Singer and Stoffers, 1980). These conditions are present in the Chew Bahir basin and the high percentage of analcime may account for the relative accumulation of potassium during arid conditions.

Ca in lake sediments mainly occurs in endogenic calcite precipitated in the water column or in biogenic carbonates (Last, 2002). Thus, we use increased XRF Ca/Ti ratio as a proxy for primarily endogenic and biogenic calcite production within the lake, while sequences with low ratios are dominated by clastic material deposition.

Carbonate nodules found in the LZ1 comprise dolomite or high-Mg and -Mn calcite. We presume that they are early diagenetic for a number of reasons. Firstly, progressive coarsening of the grain size is observed from the edge to the centre of the nodules: in the centre, there has been more time for recrystallisation and grain growth so the grains have merged into a homogeneous tightly-interlocking crystalline mass (Fig. SI-3). Secondly, the Ca/Mg ratio in the dolomite nodules is > 1; Ca-excess is a common feature of diagenetic dolomites (Armenteros, 2010; Dean et al., 2015; Vasconcelos and McKenzie, 1997). Thirdly, detrital grains are often observed as being enclosed by the carbonate, showing that the carbonate formed after the original deposition of the sediments. $\delta^{18}O$ values average + 7.3‰ across 6 dolomite nodules. These values are high, suggesting formation from high $\delta^{18}O$ water. The waters present when the dolomite and high-Mg calcite formed from the

Table 2
Luminescence dating results from Chew Bahir core HSPDP-CHB-1A measured at the Institute of Geography, University of Cologne, Germany. Dose rate data, dose distribution characteristics, De values, and OSL ages are given. mblf = meters below lake floor; PM FK = polymineral fine grains (9.8 mm aliquots); Q FK = quartz fine grains (9.8 mm aliquots); KF = potassium feldspar (1 mm aliquots); H_2O % = measured water content (water mass over dry sediment mass); U = Uranium; Th = Thorium; K = Potassium; environmental dose rate is calculated using cosmic dose calculation after Prescott and Hutton (1994) Prescott and Hutton (1994), conversion factors of Guérin et al. (2011), beta attenuation factors of Brennan (2003); internal K-content of 12.5 ± 0.5% (Huntley and Baril, 1997) and the measured water content; RSD = relative standard deviation; De = equivalent dose.

Lab code	Sample ID	Sample depth (mblf)	mineral	H_2O (%)	n accepted/	Radionuclide concentration			Dose rate (Gy/kyr)	RSD (%)	De (Gy)	Age (kyr)
					Measured aliquots	U (ppm)	Th (ppm)	K (%)				
C-L3863	CHB718	7.235–7.355	PM FK	53	10/10	2.07 ± 0.26	6.68 ± 0.39	1.96 ± 0.20	2.32 ± 0.14	5	86.5 ± 4.5	37.2 ± 3.0
C-L3864	CHB840	8.450–8.555	PM FK	34	10/20	1.57 ± 0.26	7.30 ± 0.47	2.69 ± 0.22	3.11 ± 0.18	6	120.1 ± 7.9	38.6 ± 3.4
C-L3866	CHB1617	16.365–16.520	PM FK	42	10/10	1.16 ± 0.30	6.25 ± 0.49	1.48 ± 0.12	1.87 ± 0.12	3	151.7 ± 7.7	81.2 ± 6.6
C-L3918	CHB1917	19.340–19.470	PM FK	42	11/11	1.21 ± 0.31	7.80 ± 0.49	1.62 ± 0.17	2.09 ± 0.14	4	158.7 ± 8.0	76.0 ± 6.4
C-L3867	CHB2069	19.340–19.470	PM FK	45	10/10	1.23 ± 0.31	6.62 ± 0.48	1.68 ± 0.12	1.99 ± 0.12	2	165.0 ± 8.4	82.7 ± 6.5
C-L3919	CHB2828	27.080–27.195	PM FK	31	10/10	1.48 ± 0.20	6.77 ± 0.44	1.88 ± 0.15	2.49 ± 0.15	2	224.4 ± 11.6	90.3 ± 7.1
C-L3869	CHB3140	30.420–30.535	PM FK	35	10/10	2.07 ± 0.36	9.54 ± 0.64	1.24 ± 0.13	2.32 ± 0.18	2	226.7 ± 11.6	97.9 ± 8.9
C-L3920	CHB3580	34.815–34.940	PM FK	40	12/12	3.85 ± 0.43	7.58 ± 0.49	1.05 ± 0.09	2.42 ± 0.19	5	248.7 ± 12.8	103.0 ± 10
C-L3870	CHB4140	40.570–40.690	PM FK	58	10/10	2.34 ± 0.55	10.98 ± 0.75	0.92 ± 0.10	1.99 ± 0.17	6	228.4 ± 12.3	120.0 ± 12

Table 3
List of tie-points used in the age-depth model for Chew Bahir core HSPDP-CHB-1A. Sample depths, methods and calendar ages are given. 14C = radiocarbon ages, OSL = optical stimulated luminescence ages, RPI = relative palaeointensity correlation to GLOPIS (Laj et al., 2013), ODP984 (Channell et al., 2002) and Somali Basin (Meynadier et al., 1992). mblf = metres below lake floor.

Lab code	Sample depth (mblf)	method	calendar age (kyr cal BP)
COL2915.1.1	1.44	14C	9.551 ± 0.033
C-L3863	7.30	OSL	37.2 ± 3.0
n/a	7.70	RPI	40.0 ± 1.0
C-L3864	8.50	OSL	38.6 ± 3.4
n/a	13.98	RPI	64.0 ± 2.0
C-L3866	16.44	OSL	81.2 ± 6.6
n/a	17.11	RPI	74.8 ± 3.0
C-L3918	19.41	OSL	76.0 ± 6.4
C-L3867	19.41	OSL	82.7 ± 6.5
C-L3919	27.14	OSL	90.3 ± 7.1
C-L3869	30.48	OSL	97.9 ± 8.9
C-L3920	34.88	OSL	103.0 ± 10
C-L3870	40.64	OSL	120.0 ± 12

original sediment must also have been enriched in Mg for dolomite or high-Mg calcite to form (Mazzullo, 2000). Therefore, we believe the nodules formed in a playa lake environment (Armenteros, 2010), with Mg-enriched pore waters in the sediments allowing for dolomite or high-Mg calcite formation, probably utilising Ca liberated by recrystallisation of the originally deposited endogenic calcite.

We analysed the bulk (fine fraction) calcite for stable isotopes. As discussed above, we consider the calcite to be endogenic, precipitated in the lake surface waters. The nodules, which are formed of dolomite (e.g. Fig. SI-3) and/or high-Mg/high-Mn calcite, were separated from the rest of the sediment and therefore not analysed because their isotopic composition will reflect conditions in the sediment where they formed, so isotope data would not be comparable to those from the endogenic carbonate formed in the lake waters. In terms of the drivers of endogenic calcite $\delta^{18}O$, temperature (which alone would lead to a c.0.24‰ decline in $\delta^{18}O$ for every 1 °C temperature rise) can be ruled out as the main driver in this sequence because of the magnitude of the $\delta^{18}O$ shifts. For example, the $\delta^{18}O$ change in Chew Bahir from the LGM to the Holocene is c. 6‰, and would require a temperature rise of c. 25 °C if temperature were the sole driver (Craig, 1965). This is unlikely, given the independent temperature reconstructions from elsewhere in eastern Africa for the LGM to Holocene, for example c. 6 °C in Lake Tanganyika (Tierney et al., 2008) and less (c. 3.5 °C) in Lake Malawi (Powers et al., 2005). Therefore, it is more likely that the other driver of $\delta^{18}O$ in lake carbonates, $\delta^{18}O$ of the lake water from which the carbonate forms, is the key (Leng and Marshall, 2004). In turn, this is likely to be influenced by two main factors at Chew Bahir. Firstly, in closed-basin lakes in semi-arid environments, changes in water balance lead to high magnitude changes in $\delta^{18}O$. When lake waters evaporate, $\delta^{18}O$ increases. Secondly, changes in the predominant source of precipitation, Atlantic Ocean vs. Indian Ocean/Arabian Sea, will have a lesser impact. Precipitation from the former source has to travel further and is more recycled, so $\delta^{18}O$ of the precipitation is lower by the time it reaches east Africa than precipitation from the Indian Ocean. However, the large magnitude of the shifts and, at times, the very high $\delta^{18}O$ values, suggests evaporation is the key driver (Leng and Marshall, 2004), with higher $\delta^{18}O$ indicating more evaporative lake waters, and lower $\delta^{18}O$ less evaporative lake waters. This is supported by calculated breakpoints of other aridity proxies, such as K/Ti, also suggest a shift in water balance at 66-62 kyr (c. 1380–1477 cm). Additionally, $\delta^{13}C$ supports the interpretation of a shift to drier conditions at this time (Fig. 2). $\delta^{13}C$ values of endogenic calcite can change due to variations in the composition of inflowing carbon (e.g. related to changes in catchment vegetation), within-lake productivity and the residence time of the lake (Leng and Marshall, 2004). The last of these is particularly important in closed-basin lakes such as Chew Bahir, with CO_2 preferentially degassing ^{12}C, leading to higher $\delta^{13}C$ values (Leng and Marshall, 2004). While there is only a relatively weak statistical relationship between $\delta^{18}O$ and $\delta^{13}C$, the overall trend is similar. Generally, both $\delta^{13}C$ and $\delta^{18}O$ are lower before 66 kyr and higher after 62 kyr, before lower values again at the time of the onset of the latest North African Humid period (NAHP; c. 15 kyr BP) (Figs. 2 and 6). $\delta^{13}C$, unlike $\delta^{18}O$, cannot be influenced by changes in the source of precipitation, thus the change to sustained high and stable values of both stable isotope ratios above 1380 cm core depth (LZ2) supports the interpretation of a drier, more stable hydroclimate after ~62 kyr.

The calcareous valves of lacustrine benthic ostracods are usually well preserved in sediments, unless they are exposed post-mortem to extensive transportation, chemical and/or physical weathering, which causes the dissolution or destruction of the fragile remains (Lord et al., 2012). Selective destruction of valves can alter the species composition of a thanatocoensis or eradicate the ostracod record completely (Lord et al., 2012). Thus, the generally good preservation of undamaged thin-valved ostracod valves in the presented record implies calm and constant aquatic depositional conditions at the coring location and no post-depositional reworking processes (Lord et al., 2012). A limited species diversity, as recorded in Chew Bahir with only four species, is an indication for extreme environments (for example very alkaline

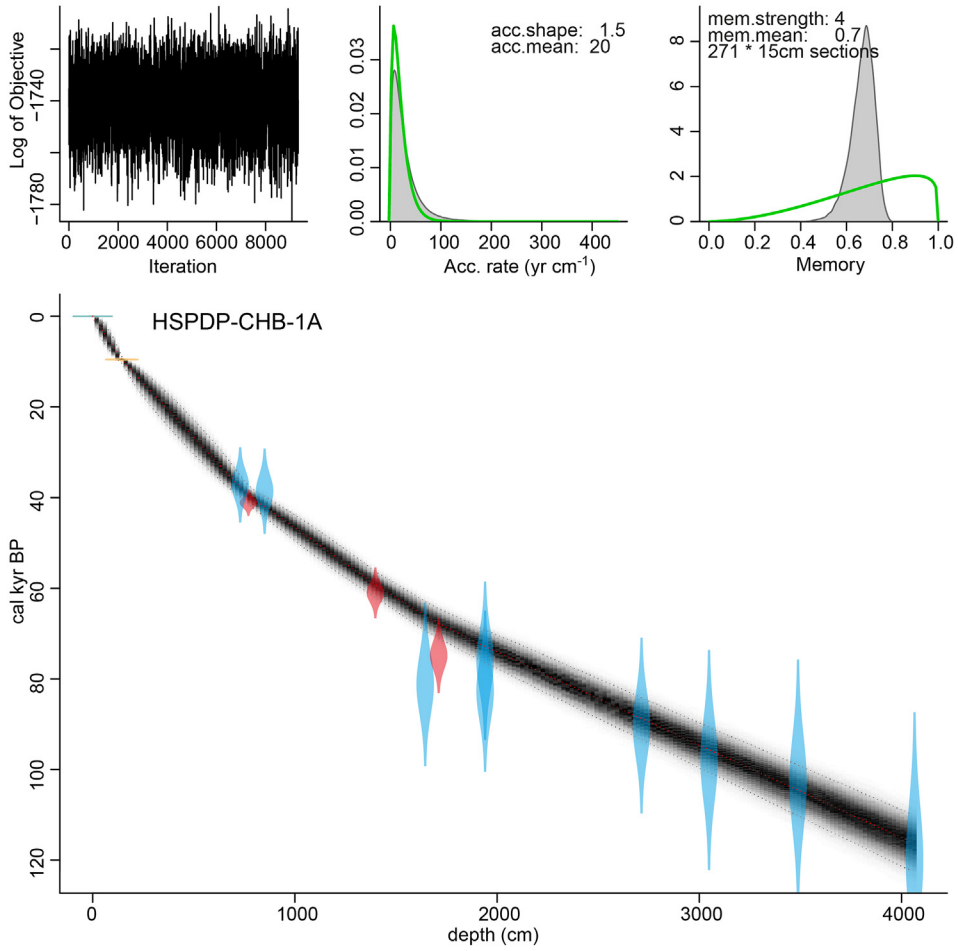

Fig. 5. Bayesian age-depth model constructed with the age-depth modelling software Bacon (Blaauw and Christen, 2011) for HSPDP-CHB-1A. Tie bars indicate ages and uncertainties from radiocarbon (orange), OSL (blue), RPI correlation (red) (see Table 3); the greyscale on the model represents the likelihood, where the darker the grey the more likely the model is of running through that section. The upper panel shows three plots (left) stability of the model; (middle) prior (line) and posterior (filled) distributions of accumulation mean; and (right) prior (line) and posterior (filled) distributions of memory properties.

waters) (Castillo-Escrivà et al., 2015). Only few ostracod species colonise playa lakes, because species need to produce either desiccation-resistant eggs (uncommon in *Limnocythere* or they have to (repeatedly) be passively transported from distant refugia (Castillo-Escrivà et al., 2015; Mesquita-Joanes et al., 2012).

4.2. Hydroclimate history of Ethiopian highlands and rift

According to our age-depth model, the core HSPDP-CHB-1A extends the environmental history of the south Ethiopian Rift and adjacent highlands to 116 kyr (Figs. 6 and 7). Previous pilot cores (Foerster et al., 2015) provide a record of the last 28 kyrs. Based on the evaluated proxies, we infer that Lake Chew Bahir reacts very sensitively to changes in hydroclimate within its catchment and that the lake basin experienced several climate cycles with a high wet-dry amplitude (Fig. 6). The lithozones of the sediment core correspond to this cyclicity. We interpret the lower element ratios, coarser grain size and increased magnetic susceptibility values in LZs 1A and 1C as detrital input by fluvial processes during wetter climate conditions, consistent with AHP4 and AHP3 of Ehrmann et al. (2016; Fig. 6). During these times especially, the Ethiopian highlands were impacted by precipitation that caused sapropel formation in the Eastern Mediterranean Sea through the freshwater discharge of the Blue Nile (Ehrmann et al., 2016; Lamb et al., 2018; Revel et al., 2010). Significant hydrological changes fostered transport and deposition of detrital terrigenous material to the basin centre of Chew Bahir (Fig. 6). Temporary lake level high stands in adjacent Lake Turkana (McDougall et al., 2008) (i.e. ~104 kyr) are likely to have occurred synchronously in Chew Bahir. Further limnogeological evidence is needed to confirm a spill over of the Chew Bahir basin to the Turkana basin (and ultimately to the White Nile catchment). Nevertheless, the presence of authigenic analcime, diagenetic nodules and lithified carbonate layers that culminate in TIC maxima in LZs 1B and 1D also reveal arid conditions between NAHPs. The high variability in $\delta^{18}O$ in this earliest part of the record before ~66 kyr also suggests large fluctuations between less and more evaporative lake waters.

The sediment record of Lake Tana in northwest Ethiopia shows similar high variability in hydroclimate on short time scales (Grove et al., 2015; Lamb et al., 2018). Likewise, further distant climate archives in north and east Africa imply episodic, but spatially nonsynchronous, wet/dry periods caused by a combination of insolation-driven shifts in the position of the ITCZ and the position of the westerlies for this time interval (Blome et al., 2012). In contrast, rapid shifts in hydroclimate during the Holocene NAHP1 are thought to be a regionally coherent feature, also connected to the Indian Ocean SST (Tierney et al., 2013). Snapshots of the Norwegian Earth System Model (NorESM) (Zhang et al., 2012; Bentsen

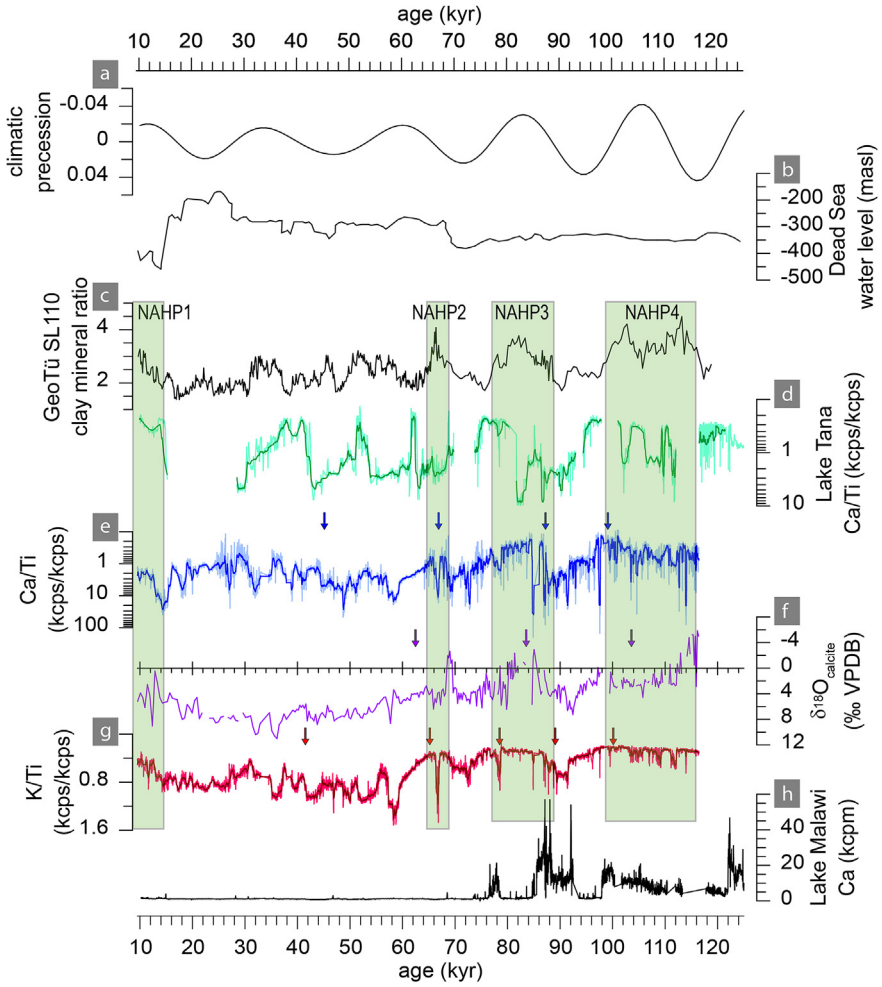

Fig. 6. Orbital cycle and palaeoenvironmental records of the Dead Sea, GeoTüSL110, HSPDP-CHB-1A, and Mal05-1C, for the last 120 kyr. a) climatic precession, b) reconstructed Dead Sea lake level (masl = metres above sea level) (Waldmann et al., 2010). c) Blue Nile runoff inferred from clay ratio [Smectite/(Illite + Chlorite)](Ehrmann et al., 2016). d) Lake level changes from Lake Tana inferred from Ca/Ti ratio (Lamb et al., 2018) (dark green - 25-point running means) e) HSPDP-CHB-1A - Ca/Ti ratio from scanning X-ray fluorescence (kcps = thousand counts per second), (dark blue - 25-point running means, arrows indicate breakpoints). f) HSPDP-CHB-1A - $\delta^{18}O$ on endogenic calcite, (magenta arrows indicate breakpoints). g) HSPDP-CHB-1A - K/Ti ratio from scanning X-ray fluorescence, arrows indicate breakpoints (dark red = 25-point running means, arrows indicate breakpoints). h) Ca relative abundance in Lake Malawi from Mal05-1C from scanning X-ray fluorescence (Lyons et al., 2015) (kcpm = thousand counts per minute).

et al., 2013) at 125 and 115 kyr (Langebroek and Nisancioglu, 2014), suggest much wetter conditions in the region of the Ethiopian highlands under high precession forcing at 125 kyr (Fig. 1b) compared to the drier conditions under low precession forcing at 115 kyr (Fig. 1c). Likewise, model simulations of intermediate complexity (CLIMBER2) (Ganopolski et al., 2001; Petoukhov et al., 2000) reproduce strong wet and arid fluctuations during MIS5 120-71 kyr (Fig. 7), which are also experienced in Lake Tana (Lamb et al., 2018). This implies that both the NorESM and the CLIMBER2 model are able to simulate the strong precipitation fluctuations of the hydroclimate in the study area. While the community climate system model (CCSM3) (Collins et al., 2006) estimates overall drier conditions for the last interglacial LIG (Otto-Bliesner et al., 2013) at 125 and 120 kyr, than experienced for the last glacial maximum (21 kyr) (Otto-Bliesner et al., 2006). Thus the proxy data from our study provide a valuable source to validate model runs for this region.

Further we interpret the peaks of K/Ti and Ca/Ti in LZs 1B and 1D as distinct drought periods at ~98-85 kyr and ~77-68 kyr, supported by the breakpoint analyses from K/Ti and Ca/Ti proxies (Fig. 6). A synchronous shift in $\delta^{18}O$ data to higher values supports the inference of highly evaporative lake waters. The LZ1B drought seems to be synchronous with extreme hydrological changes during MIS 5 in several African Rift lake basins south of Chew Bahir, e.g. lakes Naivasha (Trauth et al., 2015), Malawi (Scholz et al., 2007) and Tanganyika (Scholz et al., 2007). Here, the arid conditions led to low lake levels or even desiccation in these periods (Scholz et al., 2011; Trauth et al., 2003).

Between ~68 and 58 kyr (LZ1E), the aridity proxies (K/Ti and Ca/Ti) show a distinct sharp and steady increase to peak values and there is also a major shift to higher $\delta^{18}O$. Variable, coarser grain size suggests recurring erosional fluvial input close to the locality of the drilling site in a seasonal playa lake environment under arid conditions (Fig. 6).

We infer that a continuous lacustrine environment persisted at Chew Bahir from 58 to 32 kyr based on the presence of ostracod species. The assemblage and good preservation of autochthonous ostracod valves indicate a permanent body of water (Fig. 7). Similarly, the deposition of mainly clay/silt particles at the coring locality indicates sedimentation in a low-energy/lacustrine depositional setting (Fig. 6). Furthermore, $\delta^{18}O$ is high (+8.5 to +6.0‰) and relatively stable for tens of thousands of years, implying the existence of a body of water at Chew Bahir that was

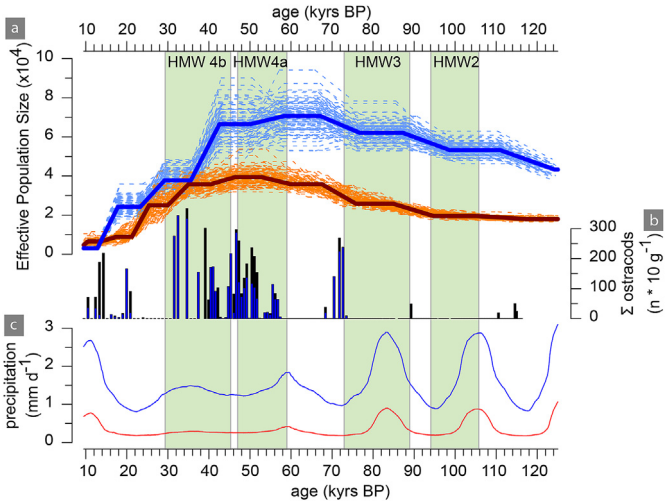

Fig. 7. Palaeoecological record of HSPDP-CHB-1A and model outcomes of precipitation and wildlife demography for the last 125 kyr. a) Modelled demographic profiles of endemic *Equus grevyi* (orange) and *Equus africanus somaliensis* (blue) (Jónsson et al., 2014). b) Ostracod valves standardised to 10 g dry-sediment; total sum (blue); *Limnocythere* cf. *borisi* (black) c) CLIMBER2 - AOV-IC model simulation of the annual mean daily precipitation (mm d^{-1}) in the Sahel grid box (blue; 10–20°N) Sahara grid box (red; 20–30°N) (cf. Fig. 1b).

subject to a substantial amount of evaporation (Leng and Marshall, 2004). This interpretation is further supported by the occurrence of analcime, which forms in highly alkaline waters in closed lake basins (Langella et al., 2001). Similarly, high K/Ti ratios correspond with deposition of clay minerals (i.e. illites and smectites), which are formed as product by physical weathering in dry conditions (Fig. 6; Foerster et al., 2018).

This period coincides with weak WAM activities in Atlantic records and declining eccentricity and a reduction in precession-dominated climate that resulted in partly high lake level stands in the Ethiopian and Afar rifts (Laskar et al., 2004; Weldeab et al., 2007). Modelled precipitation is predicted low but in less variable amounts (Ganopolski et al., 2001; Petoukhov et al., 2000). During this time, a wetter hydroclimate was also inferred from the Dead Sea records (Waldmann et al., 2010), the aforementioned southern East African Rift lakes (Scholz et al., 2007; Trauth et al., 2015) and CLIMBER2 modelled vegetation cover (Figs. 6 and 7).

4.3. Terrestrial ecosystem changes

We understand from reconstructions and modelling of population sizes of large mammals of the past hundred thousand years in eastern Africa that evolutionary or ecological changes occur on rather long time scales (Bibi and Kiessling, 2015). So, it is noteworthy that the modelled effective population size of two regionally endemic equine species peak during the time period of our reconstructed stable hydroclimate phase between ~59 and 34 kyr (Jónsson et al., 2014) (Fig. 7). *Equus grevy* (Grevy's Zebra) and *Equus africanus somali* (Somali wild ass) are arid adapted species that inhabit exclusively dry savannah habitats in the Chew Bahir region and thus being a valuable indicator species for this biome (Jónsson et al., 2014). We assume that their success is linked to the expansion of their preferred habitat in the Ethiopian Rift, which in turn was also able to support the subsistence strategies of human populations in the given region during that time interval. Following conceptual models that predict the genetic fitness of organisms (Potts and Faith, 2015) or their behavioural plasticity (Grove et al., 2015), we would expect a selection, at least in AMH, towards individuals that are adapted to a variety of different environments during the previous unstable period (Maslin et al., 2014). In the succeeding stable environment, evolved skills or at least sufficient levels of plasticity were then reached to enable dispersal out of the native habitat into distant regions with broadened habitable range (Grove et al., 2015; Potts and Faith, 2015). We therefore suggest, based on our palaeoenvironmental reconstruction presented here, that the optimal conditions for AMH emergence and dispersal from the Ethiopian rift and was most successful at the time between ~58 and 32 kyr in stable environmental conditions. This is in agreement with the evidence from archaeological records, genetic studies, and human dispersal models, which suggest a major dispersal event during the long lasting human migration wave 4 (HMW4; Mellars et al., 2013; Pagani et al., 2015; Timmermann and Friedrich, 2016). The environmental change to more stable hydroclimate coincides also with the termination of the East African Middle Stone Age industrial complex described from archaeological sites in the vicinity of Chew Bahir (Shea, 2008). This signifies a strong impact of environmental stability on the change in cultural and adaptation strategies.

A further shift to a more arid environment occurred from ~32 kyr, inferred from increased analcime formation in our sediment record, lack of ostracod valves, and persistent high K/Ti ratios (Figs. 3 and 6). This proposed playa lake environment lasted for ~10 kyrs, and also continued during the Last Glacial Maximum. Between 21 and 10 kyr, the presence of ostracod valves and the increase in detrital input from the Chew Bahir catchment (inferred from lower K/Ti ratios) suggest an increase in humidity and formation of a permanent lake again (Figs. 6 and 7). However, a distinct increase in calcite precipitation and fluctuating $\delta^{18}O$ hint to drought periods (possibly Younger Dryas) after the onset of NAHP1 (Ehrmann et al., 2016). These dramatic environmental fluctuations are also seen in previously analysed short sediment cores from Chew Bahir in more detail (Foerster et al., 2012, 2015; Trauth et al., 2015).

5. Conclusions

Using multiple proxies that record hydroclimate change, we infer extremely variable hydroclimate in Marine Isotope Stages (MIS) 5 and 4 that can be reproduced in snapshot simulations of the last interglacial (125 kyr, 115 kyr) with NorESM (Langebroek and Nisancioglu, 2014) and transient simulations (126–0 kyr) by CLIMBER2. The proxy records provides evidence of rapidly fluctuating extreme wet and arid hydroclimates. The unstable conditions are followed by stable hydroclimate around ~58 kyr at Chew Bahir. This shift was likely triggered by orbital forcing in terms of declining eccentricity and a reduction in precession-dominated climatic extremes (Mohtadi et al., 2016; Trauth et al., 2015). The timing of inferred lake water phases supports the numerical calculations of atmosphere-ocean-vegetation models of intermediate complexity and also falls in line with reconstructed wildlife population densities. We suggest from our proxy record that the optimal condition for AMH dispersal from Africa occurred ~58-32 kyr, a period of stable environments and abundant wildlife. Therefore, hydroclimate change may help explain the timing of AMH migration out of Africa.

Acknowledgements

The team members and partners from the project "Ethiopian lakes – Palaeoenvironmental Reconstruction in the Source Region of Modern Man" within the Collaborative Research Centre 806 "Our way to Europe - Culture and Environment Interaction and Human

Mobility" (CRC 806) like to take the chance to express their deepest gratitude to Henry F. Lamb for his shared knowledge and passion for palaeoenvironmental research. We feel very fortunate to have HFL in our contributing team. It is also due to his extensive international network and his expertise in Ethiopian fieldwork that the unique environmental archive of Lake Chew Bahir was successfully retrieved incl. the latest successful coring campaign within the framework of the Hominin Sites and Paleolakes Drilling Project (HSPDP). HFL's pioneer work and extensive research output is inspiring to many of us to further expand our palaeoenvironmental and palaeoclimate research.

G. Dorenbeck and Jonas Urban (University of Cologne) are thanked for support during fieldwork, and D. Klinghardt, N. Mantke, S. Opitz and numerous students (Univ. of Cologne) for their competent help in core processing. We thank A. Hu (NCAR, Boulder) for granting access to CCSM3 model data. MJL and AEM publish with permission of the Executive Director of the British Geological Survey (NERC). Financial support was provided by the German Research Foundation (DFG, Collaborative Research Centre 806), NERC (NE/K014560/1, IP/1623/0516) and ICDP-SPP 1006 (SCHA 472/13-1, 13-2, 18-1, 18-2, 18-3 & TR 419/8-1, 8-2, 10-1, 10-2, 10-3). This is publication number #17 of the Hominin Sites and Paleolakes Drilling Project (HSPDP). The data reported in this paper are available in the databases of PANGAEA and the Collaborative Research Centre 806 Database (DOI: 10.5880/SFB806.chewbahir) via http://www.crc806db.uni-koeln.de/.

Appendix A. Supplementary data

Supplementary data related to this article can be found at https://doi.org/10.1016/j.quascirev.2018.09.008.

References

Armenteros, I., 2010. Diagenesis of carbonates in continental settings. In: Alonso-Zarza, A.M., Tanner, L.H. (Eds.), Developments in Sedimentology. Elsevier, pp. 61–151.
Arnaud, F., Révillon, S., Debret, M., Revel, M., Chapron, E., Jacob, J., Giguet-Covex, C., Poulenard, J., Magny, M., 2012. Lake Bourget regional erosion patterns reconstruction reveals Holocene NW European Alps soil evolution and paleohydrology. Quat. Sci. Rev. 51, 81–92.
Assefa, Z., Yirga, S., Reed, K.E., 2008. The large-mammal fauna from the Kibish Formation. J. Hum. Evol. 55, 501–512.
Bell, W., 1980. Alpha dose attenuation in quartz grains for thermoluminescence dating. Ancient Tl 12, 8.
Bentsen, M., Bethke, I., Debernard, J.B., Iversen, T., Kirkevåg, A., Seland, Ø., Drange, H., Roelandt, C., Seierstad, I.A., Hoose, C., Kristjánsson, J.E., 2013. The Norwegian earth system model, NorESM1-M – Part 1: description and basic evaluation of the physical climate. Geosci. Model Dev. (GMD) 6, 687–720.
Bibi, F., Kiessling, W., 2015. Continuous evolutionary change in Plio-Pleistocene mammals of eastern Africa. Proc. Natl. Acad. Sci. U.S.A. 112, 10623–10628.
Blaauw, M., Christen, J.A., 2011. Flexible paleoclimate age-depth models using an autoregressive gamma process. Bayesian Analysis 457–474.
Blome, M.W., Cohen, A.S., Tryon, C.A., Brooks, A.S., Russell, J., 2012. The environmental context for the origins of modern human diversity: a synthesis of regional variability in African climate 150,000-30,000 years ago. J. Hum. Evol. 62, 563–592.
Blott, S.J., Pye, K., 2001. GRADISTAT: a grain size distribution and statistics package for the analysis of unconsolidated sediments. ESPL 26, 1237–1248.
Breeze, P.S., Groucutt, H.S., Drake, N.A., White, T.S., Jennings, R.P., Petraglia, M.D., 2016. Palaeohydrological corridors for hominin dispersals in the Middle East ~250-70,000 years ago. Quat. Sci. Rev. 144, 155–185.
Brennan, B.J., 2003. Beta doses to spherical grains. Radiat. Meas. 37, 299–303.
Brovkin, V., Bendtsen, J., Claussen, M., Ganopolski, A., Kubatzki, C., Petoukhov, V., Andreev, A., 2002. Carbon cycle, vegetation, and climate dynamics in the Holocene: experiments with the CLIMBER-2 model. GBioC 16, 86-81-86-20.
Buylaert, J.-P., Jain, M., Murray, A.S., Thomsen, K.J., Thiel, C., Sohbati, R., 2012. A robust feldspar luminescence dating method for Middle and Late Pleistocene sediments. Boreas 41, 435–451.
Castañeda, I.S., Schefuß, E., Pätzold, J., Sinninghe Damsté, J.S., Weldeab, S., Schouten, S., 2010. Millennial-scale sea surface temperature changes in the eastern Mediterranean (Nile River Delta region) over the last 27,000 years. Paleoceanography 25 (n/a-n/a).
Castillo-Escrivà, A., Valls, L., Rochera, C., Camacho, A., Mesquita-Joanes, F., 2015. Spatial and environmental analysis of an ostracod metacommunity from endorheic lakes. Aquat. Sci. 1–10.
Channell, J.E.T., Mazaud, A., Sullivan, P., Turner, S., Raymo, M.E., 2002. Geomagnetic excursions and paleointensities in the matuyama chron at ocean drilling program sites 983 and 984 (Iceland basin). J. Geophys. Res.: Solid Earth 107. EPM 1-1-EPM 1-14.
Cohen, A., Campisano, C., Arrowsmith, R., Asrat, A., Behrensmeyer, A.K., Deino, A., Feibel, C., Hill, A., Johnson, R., Kingston, J., Lamb, H., Lowenstein, T., Noren, A., Olago, D., Owen, R.B., Potts, R., Reed, K., Renaut, R., Schäbitz, F., Tiercelin, J.J., Trauth, M.H., Wynn, J., Ivory, S., Brady, K., O'Grady, R., Rodysill, J., Githiri, J., Russell, J., Foerster, V., Dommain, R., Rucina, S., Deocampo, D., Russell, J., Billingsley, A., Beck, C., Dorenbeck, G., Dullo, L., Feary, D., Garello, D., Gromig, R., Johnson, T., Junginger, A., Karanja, M., Kimburi, E., Mbuthia, A., McCartney, T., McNulty, E., Muiruri, V., Nambiro, E., Negash, E.W., Njagi, D., Wilson, J.N., Rabideaux, N., Raub, T., Sier, M.J., Smith, P., Urban, J., Warren, M., Yadeta, M., Yost, C., Zinaye, B., 2016. The Hominin Sites and Paleolakes Drilling Project: inferring the environmental context of human evolution from eastern African rift lake deposits. Sci. Drill. 21, 1–16.
Collins, W.D., Bitz, C.M., Blackmon, M.L., Bonan, G.B., Bretherton, C.S., Carton, J.A., Chang, P., Doney, S.C., Hack, J.J., Henderson, T.B., Kiehl, J.T., Large, W.G., McKenna, D.S., Santer, B.D., Smith, R.D., 2006. The community climate system model version 3 (CCSM3). J. Clim. 19, 2122–2143.
Collins, J.A., Schefuß, E., Govin, A., Mulitza, S., Tiedemann, R., 2014. Insolation and glacial-interglacial control on southwestern African hydroclimate over the past 140 000 years. EP P 398, 1–10.
Corti, G., 2009. Continental rift evolution: from rift initiation to incipient break-up in the Main Ethiopian Rift, East Africa. ESRv 96, 1–53.
Corti, G., Philippon, M., Sani, F., Keir, D., Kidane, T., 2013a. Re-orientation of the extension direction and pure extensional faulting at oblique rift margins: comparison between the Main Ethiopian Rift and laboratory experiments. Terra. Nova 25, 396–404.
Corti, G., Sani, F., Philippon, M., Sokoutis, D., Willingshofer, E., Molin, P., 2013b. Quaternary volcano-tectonic activity in the soddo region, western margin of the southern main Ethiopian rift. Tectonics 32, 861–879.
Costa, K., Russell, J., Konecky, B., Lamb, H., 2014. Isotopic reconstruction of the african Humid period and Congo air boundary migration at Lake Tana, Ethiopia. Quat. Sci. Rev. 83, 58–67.
Craig, H., 1965. The measurement of oxygen isotope palaeotemperatures. In: Tongiorgi, E. (Ed.), Stable Isotopes in Oceanographic Studies and Palaeotemperatures. Consiglio Nazionale delle Ricerche Laboratorio di Geologia Nucleare, Pisa, Italy, pp. 161–182.
Cuven, S., Francus, P., Lamoureux, S.F., 2010. Estimation of grain size variability with micro X-ray fluorescence in laminated lacustrine sediments, Cape Bounty, Canadian High Arctic. J. Paleolimnol. 44, 803–817.
Davidson, A., 1983. The Omo River Project: Reconnaissance Geology and Geochemistry of Parts of Ilubabor, Kefa, Gemu Gofa and Sidamo, Ethiopia, vol. 2. Ethiopian Institute of Geological Surveys Bulletin, pp. 1–89.
Dean, J.R., Jones, M.D., Leng, M.J., Noble, S.R., Metcalfe, S.E., Sloane, H.J., Sahy, D., Eastwood, W.J., Roberts, C.N., 2015. Eastern Mediterranean hydroclimate over the late glacial and Holocene, reconstructed from the sediments of Nar lake, central Turkey, using stable isotopes and carbonate mineralogy. Quat. Sci. Rev. 124, 162–174.
De Deckker, P., 1981. Ostracods of athalassic saline lakes. Hydrobiologia 81, 131–144.
Deplazes, G., Luckge, A., Peterson, L.C., Timmermann, A., Hamann, Y., Hughen, K.A., Rohl, U., Laj, C., Cane, M.A., Sigman, D.M., Haug, G.H., 2013. Links between tropical rainfall and North Atlantic climate during the last glacial period. Nat. Geosci. 6, 213–217.
Diro, G., Grimes, D.I.F., Black, E., 2011. Large scale features affecting Ethiopian rainfall. In: Williams, C.J.R., Kniveton, D.R. (Eds.), African Climate and Climate Change. Springer Netherlands, pp. 13–50.
Ebinger, C.J., Yemane, T., Harding, D.J., Tesfaye, S., Kelley, S., Rex, D.C., 2000. Rift deflection, migration, and propagation: linkage of the Ethiopian and eastern rifts, Africa. GSAMB 112, 163–176.
Ehrmann, W., Schmiedl, G., Seidel, M., Krüger, S., Schulz, H., 2016. A distal 140 kyr sediment record of Nile discharge and East African monsoon variability. CliPa 12, 713–727.
Foerster, V., Junginger, A., Langkamp, O., Gebru, T., Asrat, A., Umer, M., Lamb, H.F., Wennrich, V., Rethemeyer, J., Nowaczyk, N., Trauth, M.H., Schaebitz, F., 2012. Climatic change recorded in the sediments of the Chew Bahir basin, southern Ethiopia, during the last 45,000 years. Quat. Int. 274, 25–37.
Foerster, V., Vogelsang, R., Junginger, A., Asrat, A., Lamb, H.F., Viehberg, F., Trauth, M.H., Schaebitz, F., 2014. Climatic Stress Events in the Source Region of Modern Man-Matching the Last 20 Ka of the Chew Bahir Climate Record with Occupation History of Adjacent Refugia, EGU General Assembly Conference Abstracts, p. 11979.
Foerster, V., Vogelsang, R., Junginger, A., Asrat, A., Lamb, H.F., Schaebitz, F., Trauth, M.H., 2015. Environmental change and human occupation of southern Ethiopia and northern Kenya during the last 20,000 years. Quat. Sci. Rev. 129, 333–340.
Foerster, V., Deocampo, D.M., Asrat, A., Günter, C., Junginger, A., Krämer, K.H., Stroncik, N.A., Trauth, M.H., 2018. Towards an understanding of climate proxy formation in the Chew Bahir basin, southern Ethiopian Rift. Palaeogeogr. Palaeoclimatol. Palaeoecol. 501, 111–123.
Frechen, M., Schweitzer, U., Zander, A., 1996. Improvements in sample preparation for the fine grain technique. Ancient TL 14, 15–17.

Gall, Q., Hyde, R., 1989. Analcime in Lake and Lake-margin sediments of the carboniferous rocky brook formation, western newfoundland, Canada. Sedim 36, 875–887.
Ganopolski, A., Petoukhov, V., Rahmstorf, S., Brovkin, V., Claussen, M., Eliseev, A., Kubatzki, C., 2001. CLIMBER-2: a climate system model of intermediate complexity. Part II: model sensitivity. ClDy 17, 735–751.
Ganopolski, A., Calov, R., Claussen, M., 2010. Simulation of the last glacial cycle with a coupled climate ice-sheet model of intermediate complexity. Clim. Past 6, 229–244.
Goldsmith, J.R., Graf, D.L., 1958. Relation between lattice constants and composition of Ca-Mg carbonates. AmMin 43, 84–101.
Groucutt, H.S., Petraglia, M.D., Bailey, G., Scerri, E.M.L., Parton, A., Clark-Balzan, L., Jennings, R.P., Lewis, L., Blinkhorn, J., Drake, N.A., Breeze, P.S., Inglis, R.H., Devès, M.H., Meredith-Williams, M., Boivin, N., Thomas, M.G., Scally, A., 2015. Rethinking the dispersal of Homo sapiens out of Africa. Evol. Anthropol. 24, 149–164.
Grove, A.T., Street, F.A., Goudie, A.S., 1975. Former lake levels and climatic change in the rift valley of southern Ethiopia. Geogr. J. 141, 177–194.
Grove, M., Lamb, H., Roberts, H., Davies, S., Marshall, M., Bates, R., Huws, D., 2015. Climatic variability, plasticity, and dispersal: a case study from Lake Tana, Ethiopia. J. Hum. Evol. 87, 32–47.
Guérin, G., Mercier, N., Adamiec, G., 2011. Dose-rate conversion factors: update. Ancient TL 29, 5–8.
Haug, G.H., Hughen, K.A., Sigman, D.M., Peterson, L.C., Röhl, U., 2001. Southward migration of the intertropical convergence zone through the Holocene. Sciences 293, 1304–1308.
Hershkovitz, I., Weber, G.W., Quam, R., Duval, M., Grün, R., Kinsley, L., Ayalon, A., Bar-Matthews, M., Valladas, H., Mercier, N., Arsuaga, J.L., Martinón-Torres, M., Bermúdez de Castro, J.M., Fornai, C., Martín-Francés, L., Sarig, R., May, H., Krenn, V.A., Slon, V., Rodríguez, L., García, R., Lorenzo, C., Carretero, J.M., Frumkin, A., Shahack-Gross, R., Bar-Yosef Mayer, D.E., Cui, Y., Wu, X., Peled, N., Groman-Yaroslavski, I., Weissbrod, L., Yeshurun, R., Tsatskin, A., Zaidner, Y., Weinstein-Evron, M., 2018. The earliest modern humans outside Africa. Sciences 359, 456–459.
Hublin, J.-J., Ben-Ncer, A., Bailey, S.E., Freidline, S.E., Neubauer, S., Skinner, M.M., Bergmann, I., Le Cabec, A., Benazzi, S., Harvati, K., Gunz, P., 2017. New fossils from Jebel Irhoud, Morocco and the pan-african origin of Homo sapiens. Nature 546, 289.
Huntley, D.J., Baril, M.R., 1997. The K content of the K-feldspars being measured in optical dating or in thermoluminescence dating. Ancient TL 15, 11–13.
Jónsson, H., Schubert, M., Seguin-Orlando, A., Ginolhac, A., Petersen, L., Fumagalli, M., Albrechtsen, A., Petersen, B., Korneliussen, T.S., Vilstrup, J.T., Lear, T., Myka, J.L., Lundquist, J., Miller, D.C., Alfarhan, A.H., Alquraishi, S.A., Al-Rasheid, K.A.S., Stagegaard, J., Strauss, G., Bertelsen, M.F., Sicheritz-Ponten, T., Antczak, D.F., Bailey, E., Nielsen, R., Willerslev, E., Orlando, L., 2014. Speciation with gene flow in equids despite extensive chromosomal plasticity. Proc. Natl. Acad. Sci. U.S.A. 111, 18655–18660.
Junginger, A., Roller, S., Olaka, L.A., Trauth, M.H., 2014. The effects of solar irradiation changes on the migration of the Congo Air Boundary and water levels of paleo-Lake Suguta, Northern Kenya Rift, during the African Humid Period (15-5ka BP). Palaeogeogr. Palaeoclimatol. Palaeoecol. 396, 1–16.
Keir, D., Bastow, I.D., Corti, G., Mazzarini, F., Rooney, T.O., 2015. The origin of along-rift variations in faulting and magmatism in the Ethiopian Rift. Tectonics 34, 464–477.
Kelts, K., Hsü, K.J., 1978. Freshwater carbonate sedimentation. In: Lerman, A. (Ed.), Lakes: Chemistry, Geology, and Physics. Springer, New York, pp. 295–324.
Laj, C., Kissel, C., Beer, J., 2013. High resolution global paleointensity stack since 75 kyr (GLOPIS-75) calibrated to absolute values. American Geophysical Union, Timescales Of The Paleomagnetic Field, pp. 255–265.
Lamb, H.F., Bates, C.R., Bryant, C.L., Davies, S.J., Huws, D.G., Marshall, M.H., Roberts, H.M., 2018. 150,000-year palaeoclimate record from northern Ethiopia supports early, multiple dispersals of modern humans from Africa. Sci. Rep. 8, 1077.
Lane, C.S., Chorn, B.T., Johnson, T.C., 2013. Ash from the Toba supereruption in Lake Malawi shows no volcanic winter in East Africa at 75 ka. Proc. Natl. Acad. Sci. U.S.A. 110, 8025–8029.
Langebroek, P.M., Nisancioglu, K.H., 2014. Simulating last interglacial climate with NorESM: role of insolation and greenhouse gases in the timing of peak warmth. Clim. Past 10, 1305–1318.
Langella, A., Cappelletti, P., Gennaro, R.d., 2001. Zeolites in closed hydrologic systems. Rev. Mineral. Geochem. 45, 235–260.
Laskar, J., Robutel, P., Joutel, F., Gastineau, M., Correia, A.C.M., Levrard, B., 2004. A long-term numerical solution for the insolation quantities of the Earth. A&A 428, 261–285.
Last, W.M., 2002. Geolimnology of salt lakes. Geosci. J. 6, 347–369.
Lehner, B., Grill, G., 2013. Global river hydrography and network routing: baseline data and new approaches to study the world's large river systems. Hydrol. Process. 27, 2171–2186.
Leng, M.J., Marshall, J.D., 2004. Palaeoclimate interpretation of stable isotope data from lake sediment archives. Quat. Sci. Rev. 23, 811–831.
Leng, M.J., Jones, M.D., Frogley, M.R., Eastwood, W.J., Kendrick, C.P., Roberts, C.N., 2010. Detrital carbonate influences on bulk oxygen and carbon isotope composition of lacustrine sediments from the Mediterranean. Global Planet. Change 71, 175–182.
Lindroth, S., 1953. Taxonomic and Zoogeographical Studies of the Ostracod Fauna in the Inland Water of East Africa. Almqvist & Wiksells.
Lord, A.R., Boomer, I., Brouwers, E., Whittaker, J.E., 2012. Ostracod taxa as palaeoclimate indicators in the quaternary. In: Horne, D.J., Holmes, J.A., Rodriguez-Lazaro, J., Viehberg, F.A. (Eds.), Developments in Quaternary Sciences. Elsevier, pp. 37–45.
Lyons, R.P., Scholz, C.A., Cohen, A.S., King, J.W., Brown, E.T., Ivory, S.J., Johnson, T.C., Deino, A.L., Reinthal, P.N., McGlue, M.M., Blome, M.W., 2015. Continuous 1.3-million-year record of East African hydroclimate, and implications for patterns of evolution and biodiversity. Proc. Natl. Acad. Sci. Unit. States Am. 112, 15568–15573.
Mallick, S., Li, H., Lipson, M., Mathieson, I., Gymrek, M., Racimo, F., Zhao, M., Chennagiri, N., Nordenfelt, S., Tandon, A., Skoglund, P., Lazaridis, I., Sankararaman, S., Fu, Q., Rohland, N., Renaud, G., Erlich, Y., Willems, T., Gallo, C., Spence, J.P., Song, Y.S., Poletti, G., Balloux, F., van Driem, G., de Knijff, P., Romero, I.G., Jha, A.R., Behar, D.M., Bravi, C.M., Capelli, C., Hervig, T., Moreno-Estrada, A., Posukh, O.L., Balanovska, E., Balanovsky, O., Karachanak-Yankova, S., Sahakyan, H., Toncheva, D., Yepiskoposyan, L., Tyler-Smith, C., Xue, Y., Abdullah, M.S., Ruiz-Linares, A., Beall, C.M., Di Rienzo, A., Jeong, C., Starikovskaya, E.B., Metspalu, E., Parik, J., Villems, R., Henn, B.M., Hodoglugil, U., Mahley, R., Sajantila, A., Stamatoyannopoulos, G., Wee, J.T.S., Khusainova, R., Khusnutdinova, E., Litvinov, S., Ayodo, G., Comas, D., Hammer, M.F., Kivisild, T., Klitz, W., Winkler, C.A., Labuda, D., Bamshad, M., Jorde, L.B., Tishkoff, S.A., Watkins, W.S., Metspalu, M., Dryomov, S., Sukernik, R., Singh, L., Thangaraj, K., Pääbo, S., Kelso, J., Patterson, N., Reich, D., 2016. The Simons Genome Diversity Project: 300 Genomes from 142 Diverse Populations. Nature advance online publication.
Martens, K., 1984. On the freshwater ostracods (Crustacea, Ostracoda) of the Sudan, with special reference to the Red Sea Hills, including a description of a new species. Hydrobiologia 110, 137–161.
Martens, K., 1990. Revision of African *Limnocythere* s.s. Brady, 1867 (Crustacea, Ostracoda), with special reference to the Rift Valley Lakes morphology, taxonomy, evolution and (paleo)ecology. Arch. Hydrobiol. Suppl. 83, 453–524.
Martens, K., Tudorancea, C., 1991. Seasonality and spatial distribution of the ostracods of Lake Zwai, Ethiopia (Crustacea: ostracoda). Freshw. Biol. 25, 233–242.
Maslin, M.A., Brierley, C.M., Milner, A.M., Shultz, S., Trauth, M.H., Wilson, K.E., 2014. East African climate pulses and early human evolution. Quat. Sci. Rev. 101, 1–17.
Mazzullo, S.J., 2000. Organogenic dolomitization in peritidal to deep-sea sediments. J. Sediment. Res. 70, 10–23.
McDougall, I., Brown, F.H., Fleagle, J.G., 2008. Sapropels and the age of hominins Omo I and II, Kibish, Ethiopia. J. Hum. Evol. 55, 409–420.
McKenzie, K.G., 1971. Entomostraca of Aldabra, with special reference to the genus Heterocypris (Crustacea, Ostracoda). Philos. Trans. R. Soc. Lond. B Biol. Sci. 260, 257–297.
Mellars, P., Gori, K.C., Carr, M., Soares, P.A., Richards, M.B., 2013. Genetic and archaeological perspectives on the initial modern human colonization of southern Asia. Proc. Natl. Acad. Sci. U.S.A. 110, 10699–10704.
Mesquita-Joanes, F., Smith, A.J., Viehberg, F.A., 2012. The ecology of ostracoda across levels of biological organisation from individual to ecosystem: a review of recent developments and future potential. In: Horne, D.J., Holmes, J.A., Rodriguez-Lazaro, J., Viehberg, F.A. (Eds.), Developments in Quaternary Sciences. Elsevier, pp. 15–35.
Meynadier, L., Valet, J.-P., Weeks, R., Shackleton, N.J., Hagee, V.L., 1992. Relative geomagnetic intensity of the field during the last 140 ka. E&PSL 114 (1), 39–57.
Meynadier, L., Valet, J.-P., Grousset, F.E., 1995. Magnetic properties and origin of upper quaternary sediments in the Somali basin. Indian Ocean. Paleoceanography 10, 459–472.
Mohtadi, M., Prange, M., Steinke, S., 2016. Palaeoclimatic insights into forcing and response of monsoon rainfall. Nature 533, 191–199.
Nyssen, J., Poesen, J., Moeyersons, J., Deckers, J., Haile, M., Lang, A., 2004. Human impact on the environment in the Ethiopian and Eritrean highlands—a state of the art. Earth Sci. Rev. 64, 273–320.
Omondi, P., Awange, J.L., Ogallo, L.A., Okoola, R.A., Forootan, E., 2012. Decadal rainfall variability modes in observed rainfall records over East Africa and their relations to historical sea surface temperature changes. JHyd 464, 140–156.
Otto-Bliesner, B.L., Brady, E.C., Clauzet, G., Tomas, R., Levis, S., Kothavala, Z., 2006. Last glacial maximum and Holocene climate in CCSM3. J. Clim. 19, 2526–2544.
Otto-Bliesner, B.L., Rosenbloom, N., Stone, E.J., McKay, N.P., Lunt, D.J., Brady, E.C., Overpeck, J.T., 2013. How warm was the last interglacial? New model-data comparisons. Philos. Trans. R. Soc. London, Ser. A: Mathematical, Physical and Engineering Sciences 371.
Pagani, L., Schiffels, S., Gurdasani, D., Danecek, P., Scally, A., Chen, Y., Xue, Y., Haber, M., Ekong, R., Oljira, T., Mekonnen, E., Luiselli, D., Bradman, N., Bekele, E., Zalloua, P., Durbin, R., Kivisild, T., Tyler-Smith, C., 2015. Tracing the route of modern humans out of Africa by using 225 human genome sequences from Ethiopians and Egyptians. Am. J. Hum. Genet. 96, 986–991.
Pagani, L., Lawson, D.J., Jagoda, E., Mörseburg, A., Eriksson, A., Mitt, M., Clemente, F., Hudjashov, G., DeGiorgio, M., Saag, L., Wall, J.D., Cardona, A., Mägi, R., Sayres, M.A.W., Kaewert, S., Inchley, C., Scheib, C.L., Järve, M., Karmin, M., Jacobs, G.S., Antao, T., Iliescu, F.M., Kushniarevich, A., Ayub, Q., Tyler-Smith, C., Xue, Y., Yunusbayev, B., Tambets, K., Mallick, C.B., Saag, L., Pocheshkhova, E., Andriadze, G., Muller, C., Westaway, M.C., Lambert, D.M., Zoraqi, G., Turdikulova, S., Dalimova, D., Sabitov, Z., Sultana, G.N.N., Lachance, J., Tishkoff, S., Momynaliev, K., Isakova, J., Damba, L.D., Gubina, M., Nymadawa, P., Evseeva, I., Atramentova, L., Utevska, O., Ricaut, F.-X., Brucato, N., Sudoyo, H.,

Letellier, T., Cox, M.P., Barashkov, N.A., Škaro, V., Mulahasanović, L., Primorac, D., Sahakyan, H., Mormina, M., Eichstaedt, C.A., Lichman, D.V., Abdullah, S., Chaubey, G., Wee, J.T.S., Mihailov, E., Karunas, A., Litvinov, S., Khusainova, R., Ekomasova, N., Akhmetova, V., Khidiyatova, I., Marjanović, D., Yepiskoposyan, L., Behar, D.M., Balanovska, E., Metspalu, A., Derenko, M., Malyarchuk, B., Voevoda, M., Fedorova, S.A., Osipova, L.P., Lahr, M.M., Gerbault, P., Leavesley, M., Migliano, A.B., Petraglia, M., Balanovsky, O., Khusnutdinova, E.K., Metspalu, E., Thomas, M.G., Manica, A., Nielsen, R., Villems, R., Willerslev, E., Kivisild, T., Metspalu, M., 2016. Genomic analyses inform on migration events during the peopling of Eurasia. Nature 538, 238.

Petoukhov, V., Ganopolski, A., Brovkin, V., Claussen, M., Eliseev, A., Kubatzki, C., Rahmstorf, S., 2000. CLIMBER-2: a climate system model of intermediate complexity. Part I: model description and performance for present climate. ClDy 16, 1–17.

Potts, R., Faith, J.T., 2015. Alternating high and low climate variability: the context of natural selection and speciation in Plio-Pleistocene hominin evolution. J. Hum. Evol. 87, 5–20.

Powers, L.A., Johnson, T.C., Werne, J.P., Castañeda, I.S., Hopmans, E.C., Sinninghe Damsté, J.S., Schouten, S., 2005. Large temperature variability in the southern african tropics since the last glacial maximum. Geophys. Res. Lett. 32 n/a-n/a.

Prescott, J.R., Hutton, J.T., 1994. Cosmic ray contributions to dose rates for luminescence and ESR dating: large depths and long-term time variations. Radiat. Meas. 23, 497–500.

R Core Team, 2016. R: a Language and Environment for Statistical Computing. R Foundation for Statistical Computing, Vienna, Austria. https://www.R-project.org/.

Reimer, P.J., Bard, E., Bayliss, A., Beck, J.W., Blackwell, P.G., Bronk Ramsey, C., Buck, C.E., Cheng, H., Edwards, R.L., Friedrich, M., 2013. IntCal13 and Marine13 radiocarbon age calibration curves 0-50,000 years cal BP. Radiocarbon 55, 1869–1887.

Rethemeyer, J., Fülöp, R.H., Höfle, S., Wacker, L., Heinze, S., Hajdas, I., Patt, U., König, S., Stapper, B., Dewald, A., 2013. Status report on sample preparation facilities for 14C analysis at the new CologneAMS center. Nucl. Instrum. Methods Phys. Res. Sect. B Beam Interact. Mater. Atoms 294, 168–172.

Revel, M., Ducassou, E., Grousset, F.E., Bernasconi, S.M., Migeon, S., Revillon, S., Mascle, J., Murat, A., Zaragosi, S., Bosch, D., 2010. 100,000 Years of African monsoon variability recorded in sediments of the Nile margin. Quat. Sci. Rev. 29, 1342–1362.

Roberts, E.M., Stevens, N.J., O'Connor, P.M., Dirks, P.H.G.M., Gottfried, M.D., Clyde, W.C., Armstrong, R.A., Kemp, A.I.S., Hemming, S., 2012. Initiation of the western branch of the East African Rift coeval with the eastern branch. Nat. Geosci. 5, 289–294.

Scholz, C.A., Johnson, T.C., Cohen, A.S., King, J.W., Peck, J.A., Overpeck, J.T., Talbot, M.R., Brown, E.T., Kalindekafe, L., Amoako, P.Y.O., Lyons, R.P., Shanahan, T.M., Castañeda, I.S., Heil, C.W., Forman, S.L., McHargue, L.R., Beuning, K.R., Gomez, J., Pierson, J., 2007. East African megadroughts between 135 and 75 thousand years ago and bearing on early-modern human origins. Proc. Natl. Acad. Sci. U.S.A. 104, 16416–16421.

Scholz, C.A., Talbot, M.R., Brown, E.T., Lyons, R.P., 2011. Lithostratigraphy, physical properties and organic matter variability in Lake Malawi Drillcore sediments over the past 145,000 years. Palaeogeogr. Palaeoclimatol. Palaeoecol. 303, 38–50.

Shea, J.J., 2008. The middle Stone age archaeology of the lower Omo valley Kibish formation: Excavations, lithic assemblages, and inferred patterns of early Homo sapiens behavior. J. Hum. Evol. 55, 448–485.

Singer, A., Stoffers, P., 1980. Clay mineral diagenesis in two East African lake sediments. Clay Miner. 15, 291–307.

Stiles, C.A., Mora, C.I., Driese, S.G., Robinson, A.C., 2003. Distinguishing climate and time in the soil record: mass-balance trends in Vertisols from the Texas coastal prairie. Geology 31, 331–334.

Street-Perrott, F.A., Harrison, S.P., 1985. Lake levels and climate reconstruction. In: Hecht, A.D. (Ed.), Paleoclimate Analysis and Modeling. Wiley, New York, pp. 291–340.

Talbot, M.R., Kelts, K., 1986. Primary and diagenetic carbonates in the anoxic sediments of Lake Bosumtwi, Ghana. Geology 14, 912–916.

Teller, J.T., Last, W.M., 1990. Paleohydrological indicators in playas and salt lakes, with examples from Canada, Australia, and Africa. Palaeogeogr. Palaeoclimatol. Palaeoecol. 76, 215–240.

Thiel, C., Buylaert, J.-P., Murray, A., Terhorst, B., Hofer, I., Tsukamoto, S., Frechen, M., 2011. Luminescence dating of the Stratzing loess profile (Austria) - testing the potential of an elevated temperature post-IR IRSL protocol. Quat. Int. 234, 23–31.

Tierney, J.E., Russell, J.M., Huang, Y., Damste, J.S.S., Hopmans, E.C., Cohen, A.S., 2008. Northern hemisphere controls on tropical southeast African climate during the past 60,000 years. Sciences 322, 252–255.

Tierney, J.E., Smerdon, J.E., Anchukaitis, K.J., Seager, R., 2013. Multidecadal variability in east african hydroclimate controlled by the Indian Ocean. Nature 493, 389–392.

Tierney, J.E., DeMenocal, P.B., Zander, P.D., 2017. A climatic context for the out-of-Africa migration. Geology 45, 1023–1026.

Timmermann, A., Friedrich, T., 2016. Late Pleistocene Climate Drivers of Early Human Migration. Nature advance online publication.

Trauth, M.H., Deino, A., Strecker, M.R., 2001. Response of the East African climate to orbital forcing during the last interglacial (130-117 ka) and the early last glacial (117-60 ka). Geology 29, 499–502.

Trauth, M.H., Deino, A.L., Bergner, A.G.N., Strecker, M.R., 2003. East African climate change and orbital forcing during the last 175 kyr BP. EP P 206, 297–313.

Trauth, M.H., Bergner, A.G.N., Foerster, V., Junginger, A., Maslin, M.A., Schaebitz, F., 2015. Episodes of environmental stability versus instability in Late Cenozoic lake records of Eastern Africa. J. Hum. Evol. 87, 21–31.

Vasconcelos, C., McKenzie, J.A., 1997. Microbial mediation of modern dolomite precipitation and diagenesis under anoxic conditions (Lagoa Vermelha, Rio de Janeiro, Brazil). J. Sediment. Res. 67, 378–390.

Vétel, W., Le Gall, B., Walsh, J.J., 2005. Geometry and growth of an inner rift fault pattern: the Kino sogo fault belt, Turkana Rift (north Kenya). JSG 27, 2204–2222.

Waldmann, N., Torfstein, A., Stein, M., 2010. Northward intrusions of low- and mid-latitude storms across the Saharo-Arabian belt during past interglacials. Geology 38, 567–570.

Weldeab, S., Lea, D.W., Schneider, R.R., Andersen, N., 2007. 155,000 Years of West African monsoon and ocean thermal evolution. Sciences 316, 1303–1307.

Weldeab, S., Menke, V., Schmiedl, G., 2014. The pace of East African monsoon evolution during the Holocene. Geophys. Res. Lett. 41, 1724–1732.

WoldeGabriel, G., Aronson, J.L., 1987. Chow Bahir rift: a “failed” rift in southern Ethiopia. Geology 15, 430–433.

Yancheva, G., Nowaczyk, N.R., Mingram, J., Dulski, P., Schettler, G., Negendank, J.F.W., Liu, J., Sigman, D.M., Peterson, L.C., Haug, G.H., 2007. Influence of the intertropical convergence zone on the East Asian monsoon. Nature 445, 74–77.

Zeileis, A., Leisch, F., Hornik, K., Kleiber, C., 2002. Strucchange: an R package for testing for structural change in linear regression models. J. Stat. Software 1, 1–38.

Zeileis, A., Kleiber, C., Krämer, W., Hornik, K., 2003. Testing and dating of structural changes in practice. Comput. Stat. Data Anal. 44, 109–123.

Zhang, Z.S., Nisancioglu, K., Bentsen, M., Tjiputra, J., Bethke, I., Yan, Q., Risebrobakken, B., Andersson, C., Jansen, E., 2012. Pre-industrial and mid-Pliocene simulations with NorESM-L. Geosci. Model Dev 5, 523–533.